The Astrophysical Journal, 1000:112 (18pp), 2026 March 20 https://doi.org/10.3847/1538-4357/ae47dd

Gaia24ccy: An Outburst Followed the Footsteps of its Predecessor

Koshvendra Singh[1], Joe P. Ninan[1], Zhen Guo[2,3], Valentin D. Ivanov[4], David A. H. Buckley[5,6,7], Devendra K. Ojha[1], Andrew Monson[8], Tarak Chand[9,10], Saurabh Sharma[9], Ram Kesh Yadav[11], Devendra K. Sahu[12], Pramod Kumar[12], Vardan Elbakyan[13,14], Sergei Nayakshin[15], Vitor Fermiano[16], Min Fang[17,18], Jura Borissova[2,3], Wen Ping Chen[19], Franz-Josef Hambsch[20,21,22], Radostin Kurtev[2,3], Calum Morris[2,3], Javier Osses[2,3], Vania Rodríguez[2], Tanvi Sharma[19], Bandari Srikanth[12], Thanawuth Thanathibodee[23], Wei-Hao Wang[24], and Yuting Zhou[25]
[1] Department of Astronomy and Astrophysics, Tata Institute of Fundamental Research, Mumbai, 400005, India; koshvendra1999@gmail.com
[2] Instituto de Física y Astronomía, Universidad de Valparaíso, Av. Gran Bretaña 1111, Playa Ancha, Casilla 5030, Chile
[3] Millennium Institute of Astrophysics, Nuncio Monseñor Sotero Sanz 100, Of. 104, Providencia, Santiago, Chile
[4] European Southern Observatory, Karl-Schwarzschild-Strasse 2, D-85748 Garching bei München, Germany
[5] South African Astronomical Observatory, PO Box 9, Observatory 7935, Cape Town, South Africa
[6] Department of Astronomy, University of Cape Town, Private Bag X3, Rondebosch 7701, South Africa
[7] Department of Physics, University of the Free State, PO Box 339, Bloemfontein 9300, South Africa
[8] Steward Observatory and Department of Astronomy, University of Arizona, 933 N. Cherry Avenue, Tucson, AZ 85721, USA
[9] Aryabhatta Research Institute of Observational Sciences (ARIES), Manora Peak, Nainital, 263001, India
[10] M.J.P. Rohilkhand University, Bareilly, 243006, India
[11] National Astronomical Research Institute of Thailand (public organization), 260 Moo 4, T. Donkaew, A. Maerim, Chiangmai, 50180, Thailand
[12] Indian Institute of Astrophysics, II Block, Koramangala, Bangalore 560034, India
[13] Fakultät für Physik, Universität Duisburg-Essen, Lotharstraße 1, D-47057 Duisburg, Germany
[14] Research Institute of Physics, Southern Federal University, Rostov-on-Don 344090, Russia
[15] School of Physics, University of Leicester, Leicester, LE1 7RH, UK
[16] Departamento de Física, Universidade Federal de Santa Catarina, Trindade 88040-900 Florianópolis, Brazil
[17] Purple Mountain Observatory, Chinese Academy of Sciences, 10 Yuanhua Road, Nanjing 210023, People's Republic of China
[18] School of Astronomy and Space Science, University of Science and Technology of China, 96 Jinzhai Road, Hefei 230026, People's Republic of China
[19] Institute of Astronomy, National Central University, 300 Zhongda Road, Zhongli 32001 Taoyuan, Taiwan
[20] Vereniging Voor Sterrenkunde (VVS), Zeeweg 96, 8200 Brugge, Belgium
[21] Groupe Européen d'Observations Stellaires (GEOS), 23 Parc de Levesville, 28300, Bailleau lÈvêque, France
[22] Bundesdeutsche Arbeitsgemeinschaft für Veränderliche Sterne (BAV), Munsterdamm 90, 12169 Berlin, Germany
[23] Department of Physics, Faculty of Science, Chulalongkorn University, 254 Phayathai Road, Pathumwan, Bangkok 10330, Thailand
[24] Institute of Astronomy and Astrophysics, Academia Sinica, Taipei 10617, Taiwan
[25] High School Affiliated to Nanjing Normal University, 210024, Nanjing, Jiangsu Province, People's Republic of China
Received 2025 September 12; revised 2026 February 10; accepted 2026 February 17; published 2026 March 17

Abstract

Accretion-driven outbursts in young stellar objects remain poorly understood, largely limited by a statistically small sample of closely followed-up events. This underscores the importance of a thorough exploration of each outbursting object. We studied a peculiar outbursting system, Gaia24ccy, which exhibited two $\Delta g \sim 3.8$ mag outbursts in 2019 and 2024. The system consists of two unresolved, nearly identical, and rapidly rotating young stars: Gaia24ccy A (1.1419 days) and Gaia24ccy B (1.7898 days). Periodogram analyses just before the onset of the outbursts suggest Gaia24ccy B to be the outbursting component. Unlike any previously known EXor sources, the two outburst profiles show very similar evolution: both rose at the same rate for the first 15 days, followed by multiple "subbursts" on timescales of 10−20 days. The 2019 outburst lasted 145–255 days, while the 2024 outburst persisted for 367 days. We infer the unstable region to lie at $r_{\rm trigger} \simeq 0.019$–$0.047$ au ($\sim$5–12.3$R_\star$). The accreted mass per event, $M_{\rm acc} \sim 10^{-5}\ M_\odot$, can be provided by a compact inner-disk reservoir. The photometric rise and decay timescales, together with the mid-infrared (MIR) color evolution, favor a thermal–viscous trigger in a hot inner disk, while the presence of rich emission-line spectra indicates concurrent magnetospheric compression—together forming a hybrid picture. Finally, we explain the reddening of the MIR color observed during the outburst as a consequence of the competing emission from the viscous disk and the photosphere.

Unified Astronomy Thesaurus concepts: Optical bursts (1164); FU Orionis stars (553); Stellar accretion disks (1579); Protoplanetary disks (1300)

Materials only available in the online version of record: data behind figure

1. Introduction

Accretion-driven luminosity outbursts in young stellar objects (YSOs) have been proposed as solutions to various long-standing problems in low-mass star formation. These include the presence of crystalline silicates in our solar system's cometary objects (P. Ábrahám et al. 2009), the luminosity problem, in which the observed accretion rates are lower than expected from disk evolution timescales (S. J. Kenyon et al. 1990), the luminosity spread among YSOs (W. J. Fischer et al. 2023), and the presence of knots in YSO outflows (G. Ioannidis & D. Froebrich 2012). Outbursts also provide a unique window into the innermost dynamics of YSOs (K. Singh et al. 2024).

However, the triggers of these accretion bursts remain poorly understood. Various existing hypotheses predict

characteristic timescales and fluxes based on the underlying mechanisms, which can be compared with observations. One of the earliest hypotheses invoked thermal instability caused by runaway viscous heat-trapping due to hydrogen ionization in the accretion disk, leading to self-regulated accretion bursts (K. R. Bell & D. N. C. Lin 1994; S. Nayakshin et al. 2024). I. Bonnell & P. Bastien (1992) and D. J. Muñoz & D. Lai (2016) showed that circumstellar binaries in eccentric orbits can produce accretion bursts at periastron (B. M. Tofflemire et al. 2017). DQ Tau, a close binary system, has shown similar bursts (Á. Kóspál et al. 2018). Similarly, massive planets on eccentric orbits within the inner disk of a YSO can trigger accretion bursts once or twice during the rotation period (L. I. Biddle et al. 2018; J. Teyssandier & D. Lai 2020). Tidal disruption of a planet at the very inner edge of the disk could lead to a sustained accretion outburst (S. Nayakshin & G. Lodato 2012; S. Nayakshin & V. Elbakyan 2024), while stellar flybys can also trigger extreme accretion events (N. Cuello et al. 2023). Another possibility, presented by C. R. D'Angelo & H. C. Spruit (2012), involves trapping disk material at the outer edge of the magnetosphere until the ram pressure exceeds the magnetospheric pressure. Changes in the stellar dynamo cycle have also been suggested as a possible cause of accretion outbursts (P. J. Armitage 2016).

Many of these hypotheses predict periodic outbursts, highlighting such YSOs as key cases of interest. Z. Guo et al. (2022) reported 59 periodically outbursting YSOs in the near-infrared (NIR) photometric survey from the second version of the VISTA Variables in the Via Lactea Infrared Astrometric Catalogue (or VIRAC2-β; L. C. Smith et al. 2018, 2025).

2MASS J16133650-2503473 is one such object and a promising candidate for exhibiting periodic outbursts. On 2024 July 8, it was reported in *The Astronomers' Telegram* (ATel #16696; K. Sokolovsky et al. 2024) as a photometrically rising source in the All Sky Automated Survey for SuperNovae (ASAS-SN) g band. The Gaia photometric alert system independently flagged this event with the identifier Gaia24ccy. The Automatic Learning for the Rapid Classification of Events broker (or ALeRCE; F. Förster et al. 2021; P. Sánchez-Sáez et al. 2021) subsequently identified the rising source as a YSO.

Gaia24ccy subsequently exhibited an outburst with $\Delta g \approx$ 3.8 mag. We also report here, for the first time, a previously overlooked event in 2019 with essentially the same amplitude. Furthermore, the object showed a rising mid-infrared (MIR) flux (W1 and W2) around 2014, accompanied by a $\Delta V \sim 1$ mag brightening (see the "bump" in Figure 1). Figure 1 highlights the similarity between the 2019 and 2024 outbursts. Gaia24ccy thus underwent two very similar outbursts after $\sim$5 yr, with another possible candidate in 2014 (if it was missed), at an interval of 5 yr. This object is therefore an excellent candidate for investigating the mechanisms that trigger periodic accretion outbursts.

Gaia24ccy resides in the Upper Scorpius (Upper Sco) OB association, a $\sim$8–10 Myr old star-forming region (M. J. Pecaut et al. 2012; G. A. Feiden 2016; T. J. David et al. 2019), at coordinates (α_{J2000}: $16^{hr}13^{m}36\overset{s}{.}507$, δ_{J2000}: $-25^{d}03^{m}47\overset{s}{.}736$). Since Gaia Early Data Release 3 (C. A. L. Bailer-Jones et al. 2021) did not provide parallax measurement for this source, M. Fang et al. (2023) adopted the mean distance to the Upper Sco region (142 pc). We adopt the same distance in this study. K-band adaptive-optics (AO) imaging revealed that Gaia24ccy consists of two pointlike objects at a separation of 138.4 $\pm$ 1.8 mas ($\equiv$19.7 au; S. A. Barenfeld et al. 2019); see Figure 2. The two objects are of similar near-infrared (NIR) brightness, with ΔK=0.26 mag. S. A. Barenfeld et al. (2017) modeled the 0.88 mm dust continuum emission of Gaia24ccy from Atacama Large Millimeter/submillimeter Array (ALMA) observations and derived a disk inclination angle of $86^{\circ+4}_{-52}$. Treating the system as a single object, the authors also estimated an outer disk radius of 45^{-48}_{-33} au. The disk is therefore likely nearly edge-on, as also concluded by E. Nagel et al. (2024) in their study of dippers as a consequence of dust rising along the magnetospheric funnel. M. Fang et al. (2023) estimated the extinction toward the object to be $A_V = 1.3$ mag.

The paper is structured as follows. Section 2 discusses the spectroscopic and photometric data used in the work, and outlines the data-reduction and calibration procedures. Results are presented and analyzed in Section 3. We discuss and try to converge on a picture of the star-disk system and the outburst phenomenon in Section 4. We conclude the work by highlighting our key findings in Section 5. Appendices at the end of the paper provide further details of the analysis.

2. Observations and Data Reduction

In this section, we discuss the spectroscopic and photometric data acquired with various ground-based telescopes.

2.1. Hanle Faint Object Spectrograph and Camera on the 2m Himalayan Chandra Telescope

India hosts the 2 m Himalayan Chandra Telescope (HCT) at Hanle, Ladakh, in the foothills of the Himalayas. Optical spectra were obtained with the Hanle Faint Object Spectrograph and Camera (HFOSC) on the HCT. Spectra were obtained with Grating-8 (Gr8) and Grating-14 (Gr14) with a slit width of 167 μm, yielding spectral resolutions of 1200 and 1320, respectively. Gr8 and Gr14 provide a wavelength coverage of 5800–9200 Å and 3270–6160 Å, respectively. A log of the observations, along with the signal-to-noise ratios (SNRs), is provided in Table 1. The single-order spectra were reduced with IRAF (D. Tody 1986). Wavelength calibration was performed using a FeNe lamp using the corresponding grating and a 67 μm slit. The wavelength solution was further corrected by a linear fit to the Gaussian centers of various O I atmospheric lines (5577, 6300, 7913, 8344, and 8827 Å).

We constructed an instrument response function (IRF) from HFOSC observations of the telluric standard stars Feige110 and Feige34, using their flux-calibrated spectra from the CALSPEC database. This IRF was then used to correct all spectra.

We flux-calibrated the spectra by interpolating the ASAS-SN g-band photometric fluxes to the epochs of the spectra. We also analyzed other light curves to assess the photometric variability between epochs of ASAS-SN g observations. The 2024 July 13 spectrum shows an abnormally large flux toward shorter wavelengths (see Figure 3), and so it is excluded from all subsequent analysis. The flux-calibrated spectra are shown in Figure 3.

2.2. Three-hundred MilliMeter Telescope

We monitored Gaia24ccy during the first half of its outburst with the Three-hundred MilliMeter Telescope (TMMT; A. J. Monson et al. 2017) at Las Campanas Observatory, Chile. Photometric observations were performed at nearly 1 day cadence in U, B, V, R, and I bands. A total of 147, 163, 160, 159, and 162 frames were collected in the respective bands during our observation campaign from 2024 August 6 to

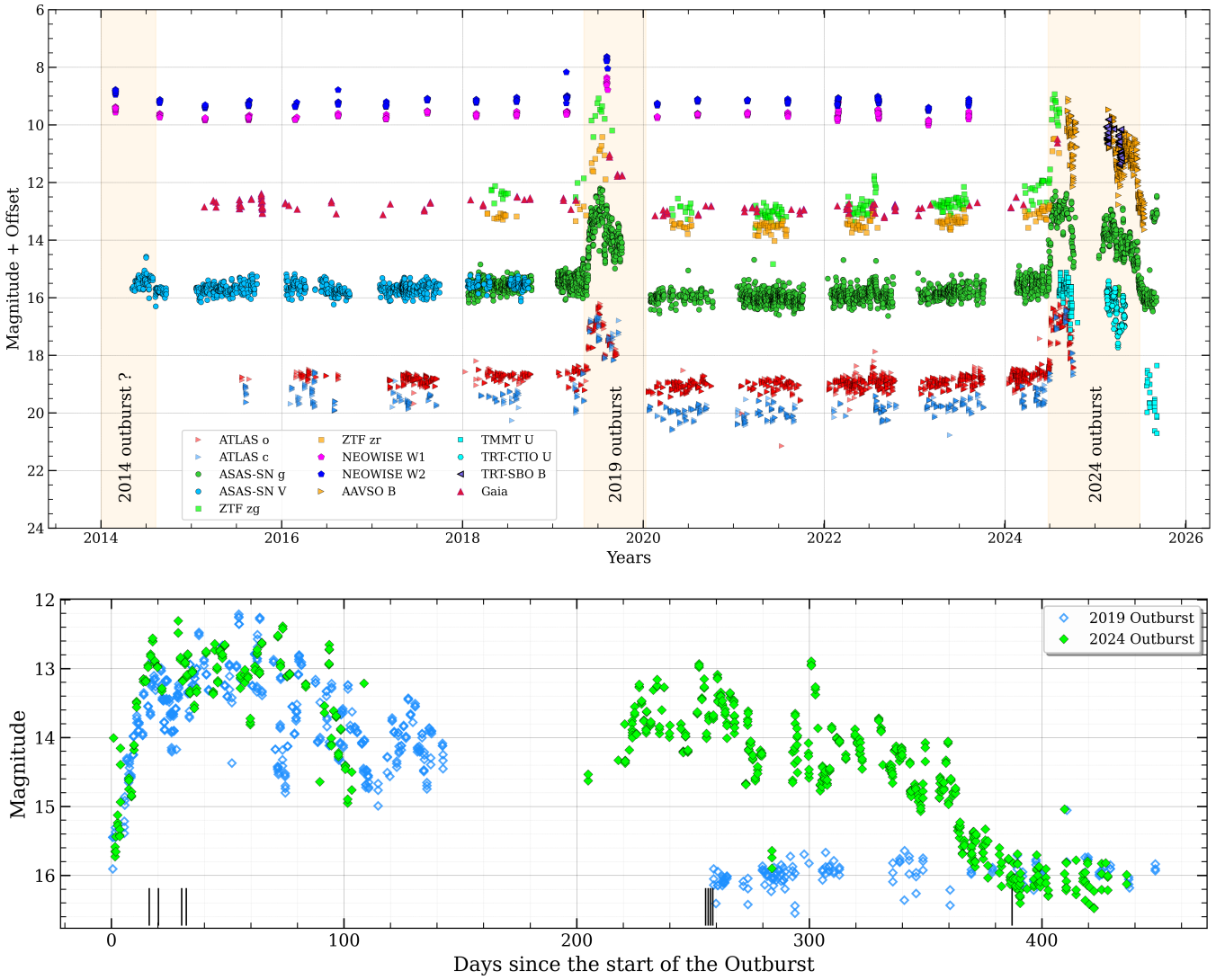

Figure 1. Upper panel: multiband light curves of Gaia24ccy, shown with magnitude offsets applied for clarity of multiwavelength evolution. Offsets are as follows: ATLAS *o* (+4.5), ATLAS *c* (+4), ASAS-SN *V* (+0.5), ZTF *r* (−1.5), ZTF *g* (−3.5), AAVSO *B* (−4), TMMT *U* (+2.5), TRT-CTIO *U* (+2.5), and TRT-SBO *B* (−4). The durations of the 2019 and 2024 outbursts are labeled and shaded with a light orange color. Light curves from other bands (AAVSO, TMMT, TRT-CTIO, and TRT-SBO) are omitted for clarity of presentation. Lower panel: the evolution of the 2019 and 2024 outbursts is shown using ASAS-SN *g*-band light curves. The start dates for the 2019 and 2024 outbursts are JD = 2458620, and 2460485, respectively. Gray vertical lines at the bottom mark the epochs of the HFOSC observations during the 2024 outburst. The photometry in this work from TMMT, LCOGT, and TRT is available in machine readable format as the data behind the figure.
(The data used to create this figure are available in the online article.)

2025 September 6. The aperture photometry of the frames was calibrated with the color equations developed from observations of four Landolt fields: SA092, SA108, SA111, and SA113 (A. U. Landolt 1992; E. Pancino et al. 2022):

$$U - B = 0.86(u - b) - 0.12(X_U - 1.5) - 1.51,$$
$$U = 0.04(U - B) - 0.36(X_U - 1.5) + 18.61 + u,$$
$$B - V = 1.29(b - v) - 0.10(X_B - 1.5) - 0.33,$$
$$B = 0.18(B - V) - 0.22(X_B - 1.5) + 20.29 + b,$$
$$V - R = 0.85(v - r) - 0.04(X_V - 1.5) - 0.05,$$
$$V = -0.14(V - R) - 0.14(X_V - 1.5) + 20.57 + v,$$
$$R - I = 0.85(r - i) - 0.05(X_R - 1.5) + 0.76,$$
$$R = -0.04(R - I) - 0.10(X_R - 1.5) + 20.64 + r,$$

where U, B, V, R, I and u, b, v, r, i are the calibrated and instrumental magnitudes, respectively. X_U, X_B, X_V, X_R are the air masses in the U, B, V, and R bands, respectively.

2.3. Las Cumbres Observatory Global Telescope

We also monitored Gaia24ccy with the Las Cumbres Observatory Global Telescope (LCOGT) network (T. M. Brown et al. 2013). We observed from 2025 February 2 to May 25, gathering a total of 157 frames, with 39, 40, 40, and 38 frames in the u, g, r, and i bands, respectively. Aperture photometry was performed on frames that had already been processed by the LCOGT pipeline. We performed differential photometry using a few reference stars in the field, adopting their calibrated magnitudes from SkyMapper (C. A. Onken et al. 2024).

2.4. Thai Robotic Telescopes

The National Astronomical Research Institute of Thailand (NARIT) operates four 0.7 m Thai Robotic Telescopes (TRT), two in each hemisphere: TRT-CTIO (Cerro Tololo Inter-

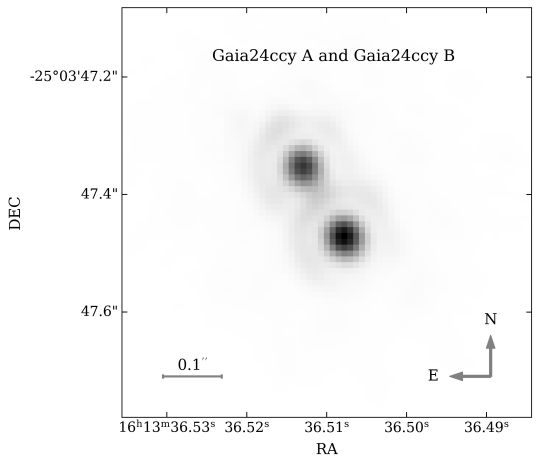

Figure 2. The *K*-band AO image of Gaia24ccy with the Near-infrared Camera, Second Generation (NIRC2) on board Keck. The image is reproduced with permission from the authors (S. A. Barenfeld et al. 2019). The two objects, with rotation periods of 1.1419 and 1.7898 days, are named Gaia24ccy A and Gaia24ccy B, respectively. Without spatially resolved rotation data, the A/B identification of the upper vs. lower component remains undetermined.

Table 1
HFOSC/HCT Logs of Gaia24ccy

JD	Exp (s)	Grating/Slit	SNR
2460501.19	600	Gr8/167 l	21
2460505.14	600,600	Gr8, Gr14/167 l, 167 l	20
2460515.21	720,720	Gr8, Gr14/167 l, 167 l	22
2460517.16	720,720	Gr8, Gr14/167 l, 167 l	20
2460740.47	1200	Gr8/167 l	30
2460741.48	1800	Gr8/167 l	38
2460742.47	1800	Gr8/167 l	50
2460743.48	1800	Gr8/167 l	46
2460872.15	1200	Gr8/167 l	10

Note. The SNR is estimated at 5700 Å.

American Observatory, Chile), TRT-SBO (Springbrook Observatory, Australia), TRT-GAO (Gaomeigu Observatory, China), and TRT-SRO (Sierra Remote Observatories, USA). From 2025 January to April, we performed U, B, V, R, I photometric observations of Gaia24ccy with TRT-CTIO and TRT-SBO. At least three frames were collected per filter in each epoch, with exposure times of 260 s (U), 120 s (B), 60 s (V), and 20 s (R and I). At TRT-CTIO, we collected 232, 231, 231, 227, and 227 frames in the $U, B, V, R,$ and I filters, respectively. At TRT-SRO, we collected 64 frames in B and 67 in each of the V, R, and I bands. The TRT pipeline produces science-ready World Coordinate System–calibrated frames after applying dark, bias, and flat-field corrections. A few filters in certain epochs were uncalibrated raw frames. We calibrated these using the concurrent calibration frames and Astrometry.net. The aperture photometry was then calibrated with secondary standards in the field of view.

2.5. All Sky Survey Light Curves

We also used multiband light curves from several surveys. These include g- and V-band light curves from the ASAS-SN (B. J. Shappee et al. 2014; C. S. Kochanek et al. 2017), B-, V-, R-, and I-band light curves from the American Association of Variable Star Observers (AAVSO), a high-cadence optical light curve from K2 (L. M. Rebull et al. 2018), and r- and g-band light curves from the Zwicky Transient Factory (ZTF; E. C. Bellm et al. 2019). Additionally, we incorporated o-band light curves from the Asteroid Terrestrial-impact Last Alert System (ATLAS; J. L. Tonry et al. 2018), W1 (3.4 μm) and W2 (4.6 μm)-band light curves from the Near-Earth Object Wide-field Infrared Survey Explorer (NEOWISE; A. Mainzer et al. 2011), and G-band light curves from Gaia (Gaia Collaboration et al. 2023).

3. Analysis and Results

In this section, we estimate the intrinsic parameters of Gaia24ccy, followed by an analysis of the outburst light-curve profiles.

Gaia24ccy is a system of two closely spaced YSOs of similar NIR brightness, Gaia24ccy A and Gaia24ccy B. We performed a Lomb–Scargle periodogram analysis on the K2 light curve (Appendix A) and identified two prominent peaks in its power spectra. We attributed the $P_A = 1.1419$ days period to Gaia24ccy A and the $P_B = 1.7898$ days period to Gaia24ccy B (Figure 2). Furthermore, Gaia24ccy B's period prominently appeared just before the two outbursts in 2019 and 2024 (Appendix B), suggesting that it is the outbursting object. In the subsequent analysis, we therefore assume that Gaia24ccy A remained in a quiescent state, while Gaia24ccy B underwent both outbursts.

3.1. Stellar Parameters

Gaia24ccy A and Gaia24ccy B have nearly identical NIR brightness, with $\Delta K = 0.26$ mag (S. A. Barenfeld et al. 2019). In the absence of additional information about the individual components, we assume that both objects are intrinsically similar during quiescence (see Section 4.1 and Appendix C).

Previous estimates of the stellar mass treated Gaia24ccy as a single object. In these studies, the stellar mass was estimated either by comparing the observed spectral flux with photospheric templates or by deriving stellar parameters from photometric fluxes (S. A. Barenfeld et al. 2016; C. F. Manara et al. 2020; L. Testi et al. 2022). Because the system consists of two objects, these studies overestimated the masses of the individual objects, Gaia24ccy A and Gaia24ccy B.

However, M. Fang et al. (2023) performed χ^2 minimization of the normalized source spectrum using normalized photospheric templates. This method depends solely on the stellar temperature and its gravity. Under our assumption that both objects are intrinsically similar, M. Fang et al. (2023) derived the spectral type (SpT) of a single object, thereby classifying Gaia24ccy A and Gaia24ccy B as M3.8 type stars.

We converted the SpT to temperature by interpolating the M1–M6 temperatures from M. Fang et al. (2017), yielding $T_\star = 3198$ K for both objects. M. Fang et al. (2023) calculated the stellar luminosity from I_{7500},[26] using bolometric corrections from G. J. Herczeg & L. A. Hillenbrand (2014). The combined stellar luminosity was $L_{\rm bol2stars} = 10^{-0.89}$ $L_\odot = 0.129$ $L_\odot$.[27] The authors then estimated the stellar mass

[26] Stellar intensity at 7500Å, calculated from the flux-calibrated spectrum. The choice of wavelength avoids a significant contribution from the excess emission of the accretion hotspot.

[27] $L_{\rm bol2stars}$ is the bolometric luminosity with equal contributions from both objects.

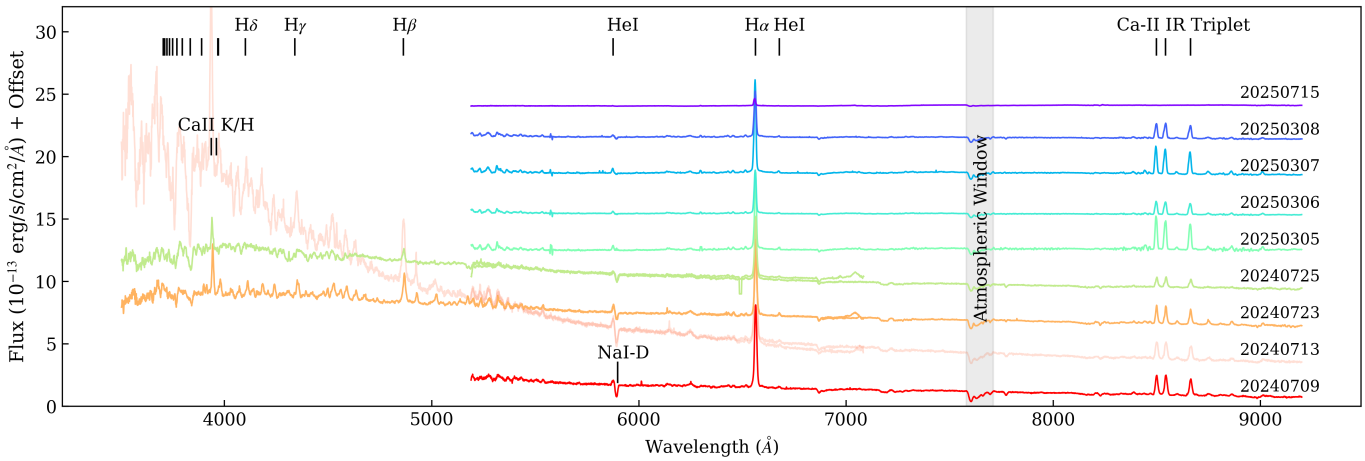

Figure 3. The flux-calibrated optical HFOSC spectra of Gaia24ccy are shown. A few prominent spectral lines are marked for reference.

using nonmagnetic pre-main-sequence tracks from G. A. Feiden (2016), together with the derived stellar temperature and luminosity. The resulting stellar mass was $M_\star = 0.20\ M_\odot$.[28] Finally, we estimated the stellar radius ($R_\star$) using the Stefan–Boltzmann relation, $L_{\rm bol} = \sigma T_\star^4 (4\pi R_\star^2)$, where σ is the Stefan–Boltzmann constant and $L_{\rm bol}$ is the bolometric luminosity of a single object. Using $L_{\rm bol} = L_{\rm bol2stars}/2 = 0.0644\ L_\odot$, we obtained $R_\star = 0.83\ R_\odot$.

We estimated the stellar parameters under the assumption that both objects are identical during quiescence, although this assumption may not hold. Future spatially resolved observations of Gaia24ccy A and Gaia24ccy B will be essential for a more robust characterization of the system.

3.2. Mass-accretion Rate

The mass-accretion rate is reliably estimated by fitting the Balmer jump of the spectrum (N. Calvet & E. Gullbring 1998; C. F. Manara 2014). Alternatively, empirical relations have been established to estimate accretion luminosities from specific spectral line fluxes and from the *U*-band excess over the stellar photosphere (E. Gullbring et al. 1998; L. Venuti et al. 2014; J. M. Alcalá et al. 2017; M. Fang et al. 2018).

C. F. Manara et al. (2020) estimated the quiescent-state mass-accretion rate ($\dot{M}_{\rm qui}$) of Gaia24ccy to be 2.93×10^{-9} $M_\odot\ {\rm yr}^{-1}$ by fitting a dereddened X-shooter spectrum with the sum of a hydrogen slab and class II photospheric templates. M. Fang et al. (2023) estimated $\dot{M}_{\rm qui} = 4.68 \times 10^{-9}\ M_\odot\ {\rm yr}^{-1}$ by calculating the accretion luminosities ($L_{\rm acc}$) from the spectral line luminosities (Hα, Hβ, HeI $\lambda\lambda$ 5876 and 6678) following the relations in M. Fang et al. (2018).[29] Under the aforementioned assumption that Gaia24ccy A and Gaia24ccy B are intrinsically similar (see Section 4.1 and Appendix C) , the quiescent mass-accretion rate of each of the sources is $2.34 \times 10^{-9}\ M_\odot\ {\rm yr}^{-1}$ (M. Fang et al. 2023).

Similarly, using our flux-calibrated HFOSC spectra, we calculated the luminosities of several spectral lines: He I 5875, Hα, Hβ, and Ca II $\lambda\lambda$ 3933, 8498, 8542, and 8662, and estimated $L_{\rm acc}$ following the relations from J. M. Alcalá et al. (2017). The spectra were dereddened for $A_V = 1.3$ mag (M. Fang et al. 2023), using the extinction curve of J. A. Cardelli et al. (1989). We estimated the mass-accretion rate ($\dot{M}_{\rm acc}$) by equating the accretion luminosity to the gravitational energy released per unit time as matter falls from a given radius ($R_{\rm in}$) onto the stellar surface:[30]

$$\dot{M}_{\rm acc} = \frac{L_{\rm acc} R_\star}{G M_\star}\left(1 - \frac{R_\star}{R_{\rm in}}\right)^{-1}, \quad (1)$$

where G is the gravitational constant, and $M_\star$ and $R_\star$ have already been defined. The inner disk radius ($R_{\rm in}$) is typically $5R_\star$ (E. Gullbring et al. 1998; G. J. Herczeg & L. A. Hillenbrand 2008). These estimates include contributions from both objects, Gaia24ccy A and Gaia24ccy B. To trace the evolution of Gaia24ccy B's accretion rate during the outburst, we subtracted the quiescent accretion rate of Gaia24ccy A from the total mass-accretion rate. The accretion rates of Gaia24ccy B are shown as colored squares and rhombuses in Figure 4 and are tabulated in Table 2. The mass-accretion rates derived from seven spectral lines show significant variation at each epoch (see Figure 4). The mass-accretion rates from Hα are consistently lower than those from photometry and other spectral lines, whereas measurements from He I 5875 Å are generally consistent with the photometric estimates, except for the second epoch. The Ca II IR triplet (Ca II IRT) lines also match the photometric measurements of $\dot{M}_{\rm acc}$, except on 2025 March 5 and 7. The quiescent accretion rate of Gaia24ccy B, estimated from the He I line in the 2025 July 15 spectrum, is $0.87 \times 10^{-9}\ M_\odot\ {\rm yr}^{-1}$, which is 2.7 times lower than that reported by M. Fang et al. (2023). However, this is consistent with the spread in the photometric mass-accretion rates during quiescence, which spans a factor of $\sim$2.2. All other spectral lines yield a total accretion rate of $1.2 \times 10^{-9}\ M_\odot\ {\rm yr}^{-1}$ for the Gaia24ccy system, implying a negative quiescent accretion rate for Gaia24ccy B. This could indicate that the H and Ca II lines originate from different regions.

[28] We note that the luminosity adopted by authors is overestimated by a factor of 2. Since the evolutionary tracks from G. A. Feiden (2016) tightly constrain the mass of late-type stars based on their photospheric temperatures, we place confidence in the stellar mass estimate of M. Fang et al. (2023).

[29] The relation coefficients in M. Fang et al. (2018) differ slightly from those in J. M. Alcalá et al. (2017), but the differences are mostly within the 1σ uncertainties.

[30] At the inner disk radius ($R_{\rm in}$), the disk is truncated by the stellar magnetic field by an equivalence of disk ram pressure and stellar magnetic pressure (J. Bouvier et al. 2007).

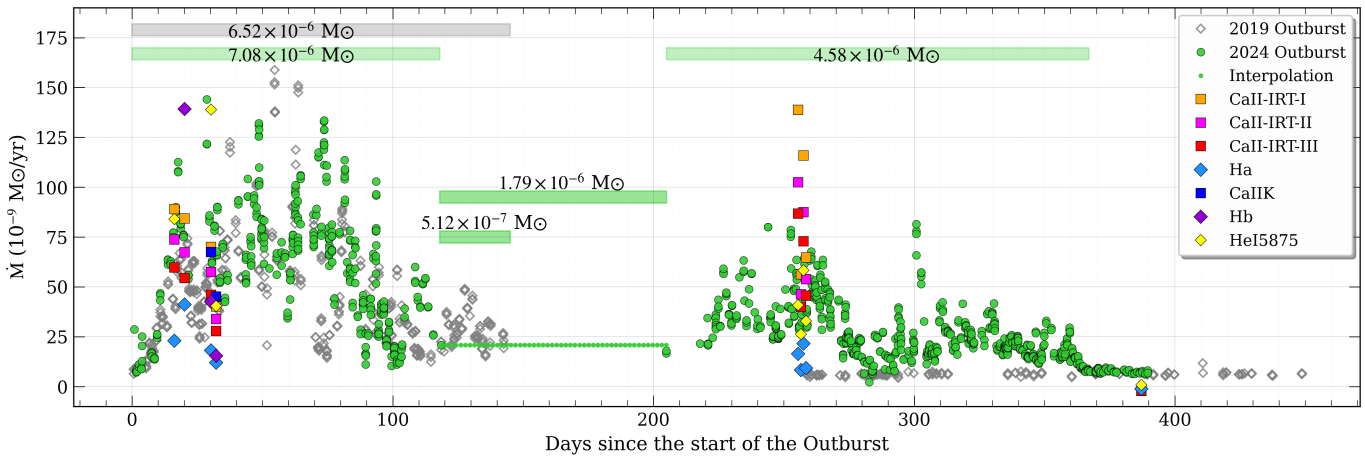

Figure 4. The accretion-rate profiles during the two outbursts of Gaia24ccy B. Gray diamonds cover the 2019 outburst, while green circles cover the 2024 outburst. The 2019 accretion profile is estimated from the ASAS-SN *g*-band light curve, while the 2024 profile is estimated from ASAS-SN *g*-band, TMMT *U*-band, LCOGT *u*-band, and AAVSO *B*-band light curves. The two halves of the 2024 outburst, before 118 days and after 205 days, are connected by linear interpolation, shown by green dots. Gray and green shaded strips highlight specific time intervals, with the accompanying text indicating the total mass accreted during each interval. The colored squares and pentagons represent mass-accretion rates estimated from the HFOSC spectral lines. The wavelengths of the Ca II IRT I, II, and III components are 8498, 8542, and 8662 Å, respectively.

Along with enhanced spectral lines, accretion manifests dramatically in the blue portion of the spectrum by releasing a significant portion of the accretion energy as an excess over the photosphere, which is captured by the *U* band (N. Calvet & E. Gullbring 1998; E. Gullbring et al. 1998). This *U*-band excess luminosity ($L_{U\text{-excess}}$) exhibits a tight correlation with the accretion luminosity (E. Gullbring et al. 1998; L. Venuti et al. 2014; Z. Guo et al. 2018; M.-T. Wang et al. 2023). We utilized our TMMT *U*-band observations obtained during the peak of the outburst to calculate the accretion luminosity. The TMMT *U*-band magnitudes were converted to flux units, using the zero-magnitude absolute flux provided by M. S. Bessell et al. (1998), and were corrected for extinction assuming $A_V = 1.3$ mag (M. Fang et al. 2023). We estimated the *U*-band excess flux by subtracting the photospheric and chromospheric contributions using an M4 spectral template of a weak-line T Tauri star (or WTTS), SZ 94, with a photospheric temperature of 3190 K (L. Ingleby et al. 2011; C. F. Manara et al. 2013, 2017; R. A. B. Claes et al. 2024). The template was reprojected to the distance of Gaia24ccy, 142 pc. Similarly, we estimated the excess flux in the ASAS-SN *g* band and established a correlation with the *U*-band excess fluxes to access high-cadence, long-term measurements of the mass-accretion rate.[31] We also derived a linear relation between the AAVSO *B*- and TMMT *U*-band excess fluxes (see Figure 5). The dereddened photometry used for establishing these correlations was observed within 2.5 hr. The coefficients did not change significantly when restricting the data to points as close as 1 hr or 0.5 hr. The relations are

$$F_{U-\text{excess}} = 1.095(\pm0.102)F_{B-\text{excess}} + 0.17(\pm0.066),$$
$$F_{U-\text{excess}} = 1.088(\pm0.063)F_{g-\text{excess}} + 0.113(\pm0.065), \quad (2)$$

where $F_{i\text{-excess}}$ is the excess flux in the *i* band over the stellar photosphere. The $F_{i\text{-excess}}$ and intercepts are given in units of 10^{-13} erg s^{-1} cm^{-2} Å^{-1}. The excess luminosity in the *U* band was then estimated following M.-T. Wang et al. (2023):

$$L_{U-\text{excess}} = 4\pi d_\star^2 \times \Delta\lambda_U \times (F_{U-\text{excess}}), \quad (3)$$

where $d_\star = 142$ pc is the distance to Gaia24ccy and $\Delta\lambda_U \sim 680$ Å is the bandwidth of the *U* filter. We estimated L_{acc} from $L_{U-\text{excess}}$ using the correlation in E. Gullbring et al. (1998), and then converted it to a mass-accretion rate via Equation (1).

L. Venuti et al. (2014) noted that accretion rates estimated from *u*-band excess luminosities following their relation were overestimated by a factor of $\leqslant$2–4 compared to those obtained with the relation of E. Gullbring et al. (1998). We tested this by calculating the mass-accretion rate from the LCOGT *u*-band excess luminosities using the relation of L. Venuti et al. (2014), and then estimating the scaling factor relative to the rates derived from Equations (2) and (3) and E. Gullbring et al. (1998). The relation is

$$\dot{M}_{\text{acc}\,-8} = 0.59(\pm0.09)\dot{M}u_{-8} - 1.27(\pm0.78), \quad (4)$$

where $\dot{M}u_{-8}$ and $\dot{M}_{\text{acc}\,-8}$ are the mass-accretion rate estimates derived from the LCOGT *u*-band and from Equation (3), respectively. $\dot{M}u_{-8}$, $\dot{M}_{\text{acc}-8}$, and the intercept are in units of $10^{-8}\,M_\odot$ yr^{-1}. The scaling factor of 0.59 is consistent with that reported by L. Venuti et al. (2014).

The uncertainties in the mass-accretion rates increased by up to ~100%. These errors are not independent for each observation epoch but are largely dominated by systematic errors propagated through the intercept of Equation (2).

Figure 4 shows the mass-accretion rate profile of Gaia24ccy B. The photometrically derived median mass-accretion rate during the preoutburst quiescence is $5.4 \times 10^{-9}\,M_\odot$ yr^{-1}, nearly twice the accretion rate estimated by M. Fang et al. (2023), $2.3 \times 10^{-9}\,M_\odot$ yr^{-1}. This quiescent rate appears overestimated, likely because the ASAS-SN g − TMMT U correlation (Equation (2)) established during the outburst may not hold during quiescence. The observation

[31] Assuming that the YSO emission is a sum of two blackbodies: the photosphere and a hotspot. Eliminating the photospheric contribution, we are left with one blackbody component. Two wavelengths of the same blackbody would produce a better-constrained linear relation. If an increase in mass-accretion rate scales with the hotspot area, we would see the same linear relation between $U_{\text{excess}} - g$, B_{excess} at various states of accretion. In contrast, the relation would be expected to change if variations in the accretion rate cause thermal variations in the hotspot.

Table 2
The Mass-accretion Rate of Gaia24ccy B from the HFOSC Spectral Lines

JD	He I 5875 Å	Hα 6563 Å	Hβ 4861 Å	Ca II K 3934 Å	Ca II IRT I 8498 Å	Ca II IRT II 8542 Å	Ca II IRT III 8662 Å
2460501.19	84.1 ± 49.9	23.0 ± 12.9	⋯	⋯	89.0 ± 68.1	73.7 ± 58.9	59.7 ± 49.7
2460505.14	224.7 ± 127.2	41.1 ± 21.6	139.2± 60.4	566.9± 256.2	84.3 ± 64.7	67.2 ± 54.2	54.4 ± 45.6
2460515.21	138.9 ± 80.3	18.1 ± 10.5	42.6 ± 20.1	67.4 ± 34.0	70.0 ± 54.3	57.4 ± 46.8	46.0 ± 39.1
2460517.16	40.4 ± 25.3	11.9 ± 7.5	15.3 ± 8.3	45.2 ± 23.5	40.2 ± 32.5	33.8 ± 28.9	27.8 ± 24.9
2460740.47	40.8 ± 25.5	16.4 ± 9.6	⋯	⋯	138.8± 104.0	102.5± 80.2	86.7 ± 70.3
2460741.48	26.3 ± 17.2	8.3 ± 5.6	⋯	⋯	56.3 ± 44.4	46.2 ± 38.4	40.0 ± 34.5
2460742.47	58.3 ± 35.5	21.6 ± 12.2	⋯	⋯	115.9± 87.5	87.5 ± 69.2	72.9 ± 59.8
2460743.48	32.9 ± 21.0	9.2 ± 6.1	⋯	⋯	64.7 ± 50.5	53.9 ± 44.1	45.6 ± 38.8
2460872.15	0.87 ± 2.1	⋯	⋯	⋯	⋯	⋯	⋯

Note. The mass-accretion rates are in units of $10^{-9}\ M_{\odot}\ \mathrm{yr}^{-1}$. We do not show the negative mass-accretion rate from the last epoch, except for the He I 5875 Å line.

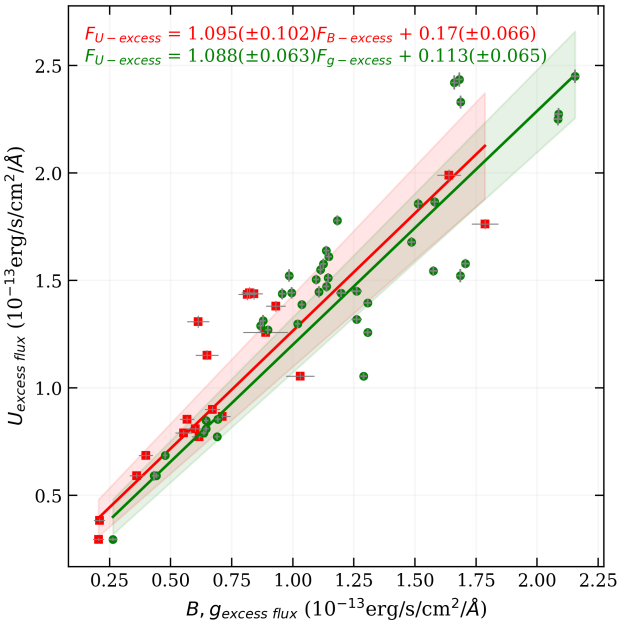

Figure 5. The linear relations between $F_{U-\mathrm{excess}}$ and $F_{B-\mathrm{excess}}$ and between $F_{U-\mathrm{excess}}$ and $F_{g-\mathrm{excess}}$ during the peak of the outburst are shown in dark red and green lines, with the 1σ uncertainties indicated by lighter shaded regions (Equation (2)). The $F_{\mathrm{i-excess}}$ and intercepts are in units of 10^{-13} erg s^{-1} cm^{-2} Å^{-1}.

reported by M. Fang et al. (2023) was obtained on 2013 June 4.

The postoutburst mass-accretion rate of the Gaia24ccy system, estimated from the TMMT U-band excess luminosity (last cyan squares in the upper panel of Figure 1), is 2×10^{-9} $M_{\odot}\ \mathrm{yr}^{-1}$ with a spread of 0.4–5 $\times$ 10^{-9} $M_{\odot}\ \mathrm{yr}^{-1}$, consistent with the estimates from C. F. Manara et al. (2020) and M. Fang et al. (2023). This spread, however, contrasts with the preoutburst quiescence, where it was only a factor of ∼2.2.

The peak accretion rates of Gaia24ccy B during the 2019 and 2024 outbursts were 1.57×10^{-7} $M_{\odot}\ \mathrm{yr}^{-1}$ and 1.42×10^{-7} $M_{\odot}\ \mathrm{yr}^{-1}$, respectively. These values are ∼67 and ∼61 times the quiescent-state value. This suggests that a naive conversion of the ratio of the photometric flux increase (33−36 ≡Δg = 3.8−3.9 mag) would have underestimated the true increase in accretion rate of the outbursting component, Gaia24ccy B, had the two objects not been resolved.

3.3. Light Curves and Outbursts

Figure 1 shows the multiband light curves of Gaia24ccy. Magnitude offsets have been applied to the light curves for clarity. As discussed earlier, the optical light curves exhibit two very similar Δg = 3.8 mag outbursts in 2019 and 2024 (shown as orange shaded regions), separated by a long period of stable brightness. The NEOWISE W1 and W2 light curves captured the 2019 outburst, showing a sharp rise. Interestingly, both the W1 and W2 light curves show a backward-rising trend around 2014, coinciding with a small, ΔV ∼ 1 mag photometric bump in the ASAS-SN light curve. This feature could represent a missed outburst (with only the tail captured) or could be regular variability, similar to the optical brightening seen in the ASAS-SN g-band light curve around 2022 June (Figure 1). Due to this ambiguity, we label the 2014 brightening event a "2014 outburst?" (with a question mark). Outbursts have recurred at least twice with an interval of ∼5 yr; a third event in 2014 remains a possibility but is unconfirmed. A future outburst in 2029 will be critical to confirm the proposed 5 yr periodicity.

3.4. 2024 Outburst: A Replica of the 2019 Outburst

The 2019 and 2024 outbursts were observed in the ASAS-SN g band, providing a direct opportunity to compare the evolution of their light-curve profiles (see lower panel in Figure 1). Figure 4 shows the corresponding mass-accretion rate profiles, with the 2019 outburst marked as gray rhombuses and the 2024 outburst as green circles.

The light curves during both outbursts rose sharply over the first 15 days, at rates of 0.160 mag day^{-1} (2019) and 0.166 mag day^{-1} (2024). This initial rise was followed by a Δg = 1.3 mag dip in 2019, while the coevolving 2024 dip is observationally incomplete. After recovering from the dip, both light curves reached a mean magnitude of ∼13 and exhibited variability over the following 45 days. The 2019 outburst light curve then underwent a sharp dip of Δg = 2 mag at 75 days; however, no similar dip was observed during the 2024 outburst. At 80 days, the light curves began a nearly linear decline, fading to g = 14.4 mag by day 100. Finally, the 2019 outburst exhibited two clear Δg ~ 1.5 mag "subbursts" (see Section 3.5) before the end of the object's annual visibility.

In 2019, when Gaia24ccy B reappeared for its annual visibility window at 255 days, it had already returned to its preoutburst quiescence level. However, in 2024, it did not return to quiescence until 367 days after the onset of the

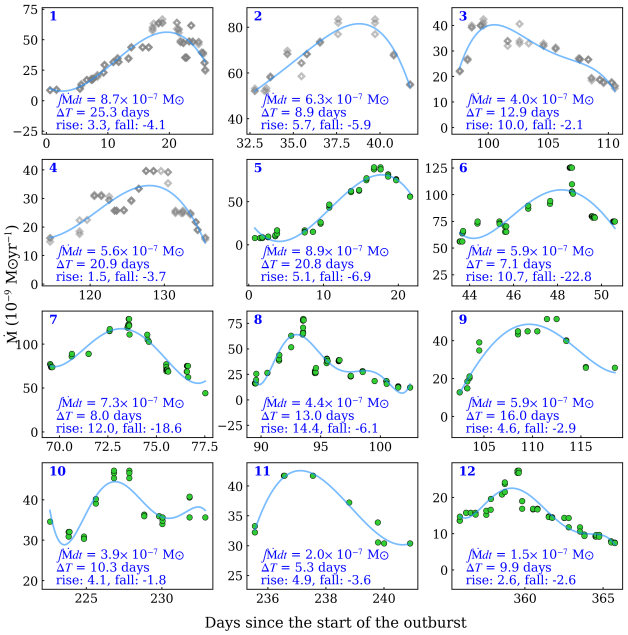

Figure 6. Subbursts during 2019 (gray rhombuses in the first and second rows) and 2024 (green circles in second, third, and fourth rows) are shown. A polynomial fit of 3°–6° is shown as a light blue curve. The timescale of the subburst (ΔT), the total mass accreted ($\int \dot{M} dt$), and the rise and fall slopes (in units of 10^{-9} $M_\odot$ yr^{-1} day^{-1}) are labeled in the respective panels. Each panel is numbered with a blue integer at the upper-left corner.

outburst. By the time the 2019 outburst had settled, the 2024 outburst was undergoing multiple $\Delta g \sim 1.2$ mag subbursts.

3.5. Subbursts during the 2019 and 2024 Outbursts

During the 2019 and 2024 outbursts, several photometric bumps of $\Delta g \sim 0.5$–1.5 mag appeared over timescales of 5–25 days, with the mass-accretion rate increasing by up to a factor of 10 (see Figures 4 and 6). These 5–25 days photometric bumps differ from the few-hour timescale clumps reported by E. Gullbring et al. (1996) and K. Singh et al. (2024). They are also longer than the rotation period at the corotation radius, that is, the radius where the Keplerian period of the disk matches the stellar period. This suggests that the events are not related to the freefall along the accretion channel or to the magnetosphere at the truncation radius, but are instead regulated by disk physics. The mechanism triggering these events could be similar to that regulating the main accretion outbursts. As aforementioned, we call these events "subbursts." We also classify the initial rise of the outburst, followed by a dip, as a subburst (see panels 1 and 5 in Figure 6 for the 2019 and 2024 outbursts, respectively).

The total mass accreted during each subburst is indicated in the corresponding panels of Figure 6. These masses may be underestimated, as portions of the events were often missed observationally. The subbursts exhibit a variety of morphologies, including slow rise and fast decay, fast rise and slow decay, and similar rates of rise and decay. The rates of rise and fall (in units of 10^{-9} $M_\odot$ yr^{-1} day^{-1}) are provided in the respective panels. S. Nayakshin et al. (2024) reported similar "subbursts" in the decaying mass-accretion rate profile of thermal-instability-driven outbursts, which the authors called "reflares."

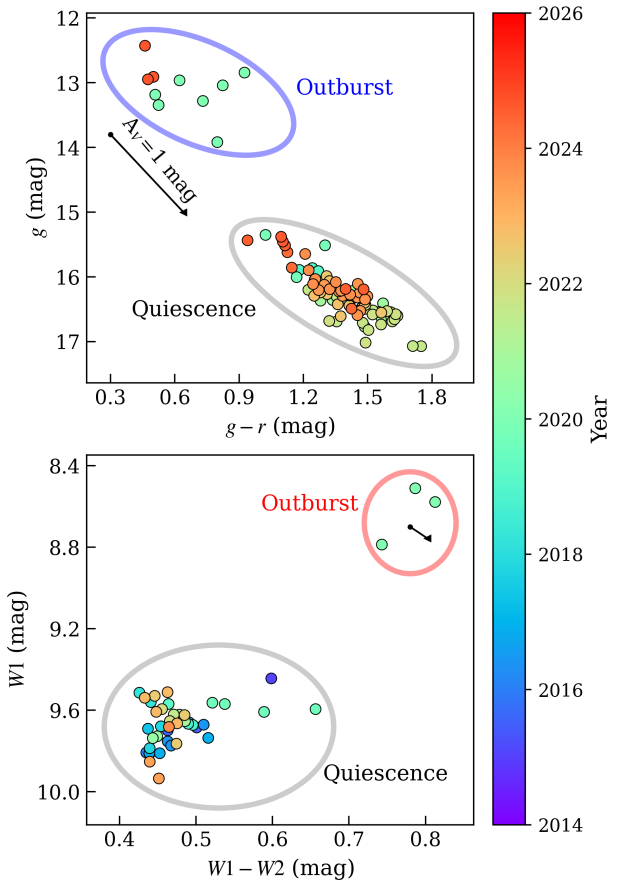

Figure 7. Upper panel: optical color–magnitude diagram shown with ZTF g- and r-band light curves. The colors of the dots represent the epoch of observation. Ellipses separately encircle the quiescence and outburst points. The lime and red dots within the outburst ellipse correspond to the 2019 and 2024 outbursts, respectively. The optical color becomes bluer during the outburst. Lower panel: MIR color–magnitude plot shown with NEOWISE W1 and W2 light curves. The MIR color becomes redder during the outburst. An extinction vector for $A_V = 1$ mag is shown.

3.6. Color Evolution: Optical Blueing and Mid-infrared Reddening during the Outbursts

The NEOWISE coverage of the 2019 outburst, together with the similar optical outburst profiles of 2019 and 2024, provides an opportunity to analyze the color evolution across both outbursts. Figure 7 shows the optical ZTF ($g - r$) and MIR NEOWISE (W1 − W2) color–magnitude diagrams across the outbursts. The optical color followed expectations for an enhanced accretion-driven event, becoming bluer as the source became photometrically brighter during both outbursts. In contrast, the MIR color reddened significantly during the 2019 outburst. Along with this secular "blueing" and reddening, Gaia24ccy B experienced regular color variations, as highlighted by the encircled points. Similar "reddening during brightening" has been reported previously by W. Park et al. (2021) and C. Morris et al. (2025). Both the optical and MIR colors exhibit significant fluctuations. During quiescence, the median optical color was $g - r = 1.42$ mag, with a range of 0.94–1.75 mag. During the outburst, the median optical color was $g - r = 0.57$ mag, with a range of 0.93–0.46 mag. The corresponding MIR colors during quiescence and outburst were 0.46 mag (range: 0.66–0.43 mag) and 0.79 mag (range: 0.81–0.74 mag), respectively. Thus, the color changes

during the outburst were $\Delta(g-r) = -0.85$ mag and $\Delta(W1-W2) = 0.33$ mag.

4. Discussion

4.1. Nature of the Two Objects: Both Are Accreting YSOs

Understanding the physical nature of Gaia24ccy A and Gaia24ccy B is crucial for interpreting key observables such as their periods, mass-accretion rates, and outburst triggers.

The NIRC2 AO image (Figure 2) revealed two nearby objects at a projected distance of 19.57 au. Both objects appeared as fast rotators in the power spectrum of the K2 light curve (Appendix A). The Lomb–Scargle periodogram analysis of the ASAS-SN light curves showed that the period of Gaia24ccy B became prominent in observation windows f (just before the 2019 outburst; see Appendix B and Appendix Figure 11) and k (just before the 2024 outburst). The appearance of Gaia24ccy B's period just before the outburst links the object directly to the event. Moreover, the median and peak-to-peak ASAS-SN g flux levels increased in these two windows with respect to the preceding quiescent-state windows, e and j. The simultaneous rise of both mean and peak-to-peak fluxes suggests that the hotspot contribution from Gaia24ccy B to the total flux was amplified. The photometric rise (and so enhanced accretion rate), even before the actual onset of the outburst indicates that Gaia24ccy B is the outbursting object. Since Gaia24ccy B underwent two outbursts, it is an accreting object and hence a YSO.

The dips in the K2 light curve (see Appendix C) provide insights into the nature of the second object. Appendix C suggests that the dips could possibly result from quasiperiodic occultations of Gaia24ccy A. Such dips have been reported earlier and are well studied (see, e.g., J. Bouvier et al. 1999). Previous studies suggest two main explanations for the dips: (i) occultation of the central star by warps in the disk material near the corotation radius (J. Bouvier et al. 1999), and (ii) periodic occultation by dust material from the disk rising along the magnetosphere, which temporarily blocks the star as viewed along the accretion funnel (or hotspot if there is no azimuthal twisting of the funnel; E. Nagel et al. 2024). Both scenarios require the object to have a surrounding highly inclined disk, allowing for occultation of the central object. This suggests the possibility that Gaia24ccy A also harbors a circumstellar disk and is undergoing accretion. Thus, for the purposes of this study, we assume that Gaia24ccy A is also a YSO with a highly inclined disk.

4.2. On Outburst-triggering Mechanism

Figure 4 shows that the outbursts' profiles remained similar for at least 100 days after onset. The comparable timescales and fluxes suggest that the initial disk conditions leading to the outbursts could have been remarkably similar, even after 5 yr. The repeatability of the outbursts rules out irregular external triggers, such as the infall of accretion streams onto the disk or stellar flybys (M. Kuffmeier et al. 2018; E. M. A. Borchert et al. 2022).

In a potential binary system, Gaia24ccy A could trigger a gravitational instability in the inner disk of Gaia24ccy B at periastron, initiating an accretion outburst (B. M. Tofflemire et al. 2017; N. Cuello et al. 2023). However, if the two objects are in a circular orbit with a radius equal to their current projected separation of 19.57 au, Kepler's third law of motion suggests an orbital period of ≈137 yr. This suggests that the objects would move by only 13° over the 5 yr, making this trigger mechanism unlikely.

Among regular external perturbations, a planet in an eccentric orbit with a period of ∼5 yr could gravitationally perturb the disk at periastron. Such a planet would have an orbital radius of 1.71 au.

Two intrinsic mechanisms, however, provide more natural explanations for repeated bursts in a replenishable inner disk, and are discussed below. The first is a thermal–viscous instability (TI), in which a local heating–cooling imbalance (often aided by mass pileup or a change in effective viscosity) drives a disk annulus into a hot, high-viscosity state, producing an outburst (K. R. Bell & D. N. C. Lin 1994). The second is magnetospheric gated-accretion, the so-called D'Angelo–Spruit (DS) mechanism (C. R. D'Angelo & H. C. Spruit 2012), in which material accumulates at the magnetospheric truncation radius (R_T) and is released episodically onto the star. Below, we treat TI and magnetospheric/DS scenarios as distinct, testable possibilities.

We use "initial conditions" in two distinct senses. For the TI scenario, this refers to the local thermal and viscous state (temperature, surface density, ionization) at the unstable radius. For the DS/gated-accretion scenario, it refers to the accumulation (pileup) of mass and pressure at the magnetospheric boundary. Below, we treat these two meanings separately and present diagnostics appropriate to each.

4.2.1. Reset Mechanism

The remarkable resemblance between the two outburst profiles and the similar rate of rise during the first 15 days suggests that the outbursts could have been triggered by similar initial conditions at the same disk radius on both occasions. The two similar outbursts are separated by ≈5 yr; this recurrence could reflect either a characteristic replenishment timescale in the outer disk or be coincidental. We cannot establish periodicity from two events. Therefore, below we consider multiple physical scenarios that could produce similar repeated bursts.

Figure 4 shows the amount of matter accreted during each outburst. In the 2019 outburst, Gaia24ccy B accreted $6.52 \times 10^{-6}\,M_{\odot}$ within 145 days after the onset. By 255 days after the outburst, the star had returned to quiescence. Similarly, $7.08 \times 10^{-6}\,M_{\odot}$ of matter was accreted during the first 120 days of the 2024 outburst. To compare accretion over similar durations for the 2019 and 2024 outbursts, we linearly interpolated the 2024 accretion-rate profile from day 118 to 205 (green dots in Figure 4). Accounting for the additional 25 days from the interpolation, the total accreted material during the 2024 outburst is estimated at $7.59 \times 10^{-6}\,M_{\odot}$. If a subburst occurred during those 25 days, it could have added $8\text{–}9 \times 10^{-7}\,M_{\odot}$ (maximum mass in Figure 6), resulting in a total accreted mass of $7.88\text{–}7.98 \times 10^{-6}\,M_{\odot}$ during the first 145 days of the 2024 outburst. This suggests that a similar amount of matter was accreted onto Gaia24ccy B during the first 145 days of both outbursts, with the slight difference attributed to the observational cadence. This accreted mass represents the lower limit on the critical mass ($M_{\rm critical}$, corresponding to the observed limiting duration of the 2019 outburst) required to trigger the outburst, such that

$M_{\rm critical} = 7.6 \times 10^{-6}\,M_{\odot}$.

The Accumulation of $7.6 \times 10^{-6}\ M_{\odot}$ of mass would have reset the initial conditions that triggered the outburst at a specific disk radius, $r_{\rm trigger}$.

4.3. Timescales, Mass Budget, and Diagnostics for TI versus DS

The orbital periods and Keplerian frequencies in the very inner disk are short; for example, the Keplerian period is ∼0.3 days at $r \simeq 1.3R_{\star}$, ∼2.2 days at $r \simeq 5R_{\star}$, ∼2.9 days at $r \simeq 6R_{\star}$, and ∼14.4 days at $r \simeq 17.2R_{\star}$. These short dynamical times ($1/\Omega(r)$, where $\Omega(r) = \sqrt{GM\star/r^3}$ is the angular speed) set the minimum possible rise times for any process operating at small radii.

4.3.1. Timescales: Definitions and Diagnostic Use

For the purposes of diagnosing the outburst mechanism, we distinguish two characteristic timescales. The decay of an outburst is governed by the hot-state viscous time at the outer edge of the unstable region (W. J. Fischer et al. 2023):

$$t_{\nu}(r) = \frac{r^{3/2}}{\alpha h^2 \sqrt{GM_{\star}}}, \qquad h \equiv \frac{H}{r}, \tag{5}$$

where α is a dimensionless viscosity parameter and H is the disk scale height at disk radius r. The rise is set by the (local) thermal time:

$$t_{\rm th}(r) = \frac{1}{\alpha \Omega(r)}. \tag{6}$$

Eliminating α between Equations (5) and (6) gives a direct link between the thermal and viscous times:

$$\frac{t_{\nu}}{t_{\rm th}} = \frac{1}{h^2} \quad \Rightarrow \quad h = \sqrt{\frac{t_{\rm th}}{t_{\nu}}}, \tag{7}$$

which we use below to infer the inner-disk aspect ratio (h) from the observed rise and decay timescales.

It must be emphasized that the observable photometric rise is generally longer than the local thermal time because heating fronts have finite widths and finite propagation speeds and because ionization energy must be supplied in the transition region; heating-front simulations therefore show that measured rises correspond to several local thermal times rather than exactly one $t_{\rm th}$ (K. R. Bell & D. N. C. Lin 1994; J.-M. Hameury et al. 1998; K. Menou et al. 1999; G. Dubus et al. 2001). To conservatively bracket this effect, we adopt

$$t_{\rm th} \simeq \frac{t_{\rm rise}}{f}, \qquad f \in [2, 5], \tag{8}$$

i.e., the photometric rise is assumed to be a few times the local thermal time; the range $f = 2$–5 reflects the spread of behaviors seen in heating-front calculations (J.-M. Hameury et al. 1998; K. Menou et al. 1999).

4.3.2. Numerical Estimates Using the Decay Time

We use only the observed decay time as the proxy for the viscous time t_{ν}. For the 2024 event, the measured decay is $t_{\rm decay} \simeq 350$ days; for the 2019 event, the available coverage gives limiting decay values in the range $t_{\rm decay} \simeq 128$–238 days. With $t_{\rm rise} \simeq 17$ days and $t_{\rm th} = t_{\rm rise}/f$, we infer the disk aspect ratio $h = \sqrt{t_{\rm th}/t_{\nu}}$.

For the 2024 decay, $t_{\nu} = t_{\rm decay} = 350$ days and $t_{\rm rise} = 17$ days, we obtain, taking $f \in [2, 5]$,

$$t_{\rm th} \in [3.4,\ 8.5]\ \text{days} \quad \Rightarrow \quad h = \sqrt{\frac{t_{\rm th}}{t_{\nu}}} \simeq 0.10\text{–}0.16, \tag{9}$$

with a central value $h \approx \sqrt{5.67/350} \simeq 0.13$ for $f = 3$.

Applying the same procedure to the 2019 limiting decays gives larger aspect ratios; for $t_{\rm decay} = 128$ days, we find $h \sim 0.16$–0.26 (central ∼0.21 for $f = 3$), while for $t_{\rm decay} = 238$ days, we obtain $h \sim 0.12$–0.19 (central ∼0.15 for $f = 3$). Thus, the 2024 event implies a hot-state aspect ratio $h \sim 0.10$–0.16, plausibly in the range expected for a thermally ionized, magnetorotational instability (MRI)-active inner disk, whereas explaining the shortest 2019 decay requires either a more strongly puffed-up hot disk or a smaller effective radius for the unstable region during that epoch.

4.3.3. Expected Behavior of DS and TI and Quick Comparison with the Observations

The magnetospheric gated-accretion scenario differs from TI in the physical locus and typical timescales. In DS, the stellar magnetosphere truncates the inner disk at R_T, where material supplied from larger radii piles up and is released episodically when the barrier is overcome (C. R. D'Angelo & H. C. Spruit 2012). The buildup interval is set by the supply to R_T, the rise is often rapid (dynamical or magnetospheric timescales near R_T), and the decay is governed by viscous draining of the innermost region. If R_T collapses to very small radii during outburst, DS-driven bursts can have very fast rises (hours to days) and relatively short decays (weeks to months), depending on the hot-state viscosity.

By contrast, TI is a local thermal–viscous runaway, where the observable rise is controlled by heating-front propagation and the decay is determined by the viscous time at the outer edge of the unstable zone (K. R. Bell & D. N. C. Lin 1994). Consequently, TI naturally produces longer-duration events (months to years) when the unstable region extends over several stellar radii, and the mass accreted corresponds to that contained in the unstable annulus.

Comparing these expectations with the data, the measured rise of ∼17 days and the 2024 decay of ∼350 days are readily accommodated by TI for plausible hot-state parameters ($\alpha_{\rm hot} \sim 0.05$–0.15, $h \sim 0.1$). The shorter 2019 decay (128–238 days) can still be reconciled with TI only if the hot-state disk was substantially puffed up, the effective unstable radius was smaller, or if the observed section of the event captured only part of a longer viscous decay. Below, we estimate the $r_{\rm trigger}$ from Equation (5) for plausible values of α within the estimated range of h. For comparison, the corotation radius of Gaia24ccy B is $4.73R_{\star} \equiv 0.017$ au.

For the 2024 outburst, $t_{\nu} = t_{\rm decay} = 350$ days, and $h = 0.10$–0.16:

1. $\alpha = 0.05 \Rightarrow 3.2R_{\star} \leqslant r_{\rm trigger} \leqslant 5.9R_{\star}$;
2. $\alpha = 0.10 \Rightarrow 5.0R_{\star} \leqslant r_{\rm trigger} \leqslant 9.4R_{\star}$;
3. $\alpha = 0.15 \Rightarrow 6.6R_{\star} \leqslant r_{\rm trigger} \leqslant 12.3R_{\star}$.

For the 2019 outburst, $t_{\nu} = t_{\rm decay} = 128$ days, and $h = 0.16$–0.26:

1. $\alpha = 0.05 \Rightarrow 3.0R_{\star} \leqslant r_{\rm trigger} \leqslant 5.8R_{\star}$;
2. $\alpha = 0.10 \Rightarrow 4.0R_{\star} \leqslant r_{\rm trigger} \leqslant 9.2R_{\star}$;
3. $\alpha = 0.15 \Rightarrow 6.3R_{\star} \leqslant r_{\rm trigger} \leqslant 12.0R_{\star}$.

For the 2019 outburst, $t_\nu = t_{\rm decay} = 238$ days, and $h = 0.12$–0.19:

1. $\alpha = 0.05 \Rightarrow 3.1R_\star \leqslant r_{\rm trigger} \leqslant 5.75R_\star$;
2. $\alpha = 0.10 \Rightarrow 4.9R_\star \leqslant r_{\rm trigger} \leqslant 9.1R_\star$;
3. $\alpha = 0.15 \Rightarrow 6.5R_\star \leqslant r_{\rm trigger} \leqslant 12.0R_\star$.

DS remains viable—especially if, during outburst, the truncation radius moves very close to the star and releases a relatively small pileup mass—but the numerical timescale and aspect-ratio estimates suggest that TI is a plausible primary mechanism for the longer 2024 event.

Within the TI framework, adopting $\alpha_{\rm quiescence} = 0.04$, the outburst repeating timescale around a 0.2 $M_\odot$ star is ≈5.4 yr (Equation (20) in S. Nayakshin et al. 2024), comparable to the ∼5 yr separation between the two outbursts of Gaia24ccy B, should future observations establish this as an outburst recurrence timescale.

4.3.4. Mass Reservoir

The total accreted mass per event is $M_{\rm acc} \simeq 10^{-5}\ M_\odot$ ($\approx 2 \times 10^{28}$ g). The integrated mass-accretion rate for the observed duration of 2024 outburst is $1.3 \times 10^{-5}\ M_\odot$ (from Figure 4), while the lower limit of the total accreted mass during the 2019 outburst is $6.5 \times 10^{-6}\ M_\odot$. In the TI picture, this mass must come from the unstable annulus: A simple estimate of the mean surface density required, $\bar{\Sigma} \simeq M_{\rm acc}/(\pi r^2)$, evaluated at $r \simeq 6R_\star$ gives $\bar{\Sigma} \sim 5.3 \times 10^4$ g cm^{-2}, and for $r_{\rm trigger} = 12R_\star$ it is $\bar{\Sigma} \sim 1.3 \times 10^4$ g cm^{-2}. While large, this value is not implausible for the very inner regions of a young disk, and TI operating over a realistic annulus width (e.g., $\Delta r \sim 0.2 - 0.4R_\star$) can comfortably supply $\sim 10^{-6}$–10^{-5} $M_\odot$. In the DS picture, the released mass corresponds to the pileup at R_T; DS naturally accommodates small-to-moderate masses per burst (Earth-mass scale to super-Earth scale), and therefore the measured $M_{\rm acc}$ is fully consistent with a single DS release. Thus, mass-budget arguments alone do not uniquely distinguish between TI and DS.

However, the recurrence time provides an additional constraint. The two observed outbursts are separated by ∼5 yr, where the quiescent accretion rate onto the star is orders of magnitude lower than the burst accretion rate. If the total accreted mass ($M_{\rm acc}$), piled up at $r_{\rm trigger}$, were supplied steadily from the outer disk, the accretion rate beyond $r_{\rm trigger}$ would be $\simeq 2 \times 10^{-6}\ M_\odot$ yr^{-1}. Considering $M_{\rm critical}$ as the threshold pileup mass, $\dot{M}_{r>r_{\rm trigger}} = 1.5 \times 10^{-6}\ M_\odot$ yr^{-1}. This exceeds the peak accretion rate onto the star during the outburst. Therefore, the accumulated mass would always exceed $M_{\rm critical}$, leading to a sustained or quasi-continuous outburst, which is not observed. Instead, the system undergoes discrete events that rapidly drain the accumulated reservoir over 145–367 days. This suggests that the accretion rate beyond $r_{\rm trigger}$ is nonsteady or episodic.

With $\dot{M}_{r>r_{\rm trigger}} = 1.5 \times 10^{-6}\ M_\odot$ yr^{-1}, Equation (15) of S. Nayakshin et al. (2024) suggests $r_{\rm trigger} \approx 0.043$ au $\equiv 11.3R_\star$, consistent with the estimates in Section 4.3.3.

In both the TI and DS pictures, some form of temporary mass storage is required: In TI, mass builds up locally until a thermal runaway is triggered, while in DS the accumulation occurs near the truncation radius until magnetospheric conditions allow rapid release. Thus, while the mass reservoir alone does not discriminate between mechanisms, the combination of discrete recurrence, rapid draining, and low quiescent accretion strongly favors scenarios involving episodic inner-disk mass accumulation rather than steady inflow.

4.3.5. Magnetospheric Evolution and Spectral Diagnostics

The magnetospheric truncation radius scales as $R_T \propto \dot{M}^{-2/7}$ (J. Bouvier et al. 2007). The quiescent and peak accretion rates ($\dot{M}_{\rm q} = 2.34 \times 10^{-9}\ M_\odot$ yr^{-1} and $\dot{M}_{\rm peak} = 1.74 \times 10^{-7}\ M_\odot$ yr^{-1}, respectively) yield

$$\frac{R_{T,\rm outburst\ peak}}{R_{T,\rm q}} = \left(\frac{\dot{M}_{\rm q}}{\dot{M}_{\rm outburst\ peak}}\right)^{2/7} \simeq 0.29, \qquad (10)$$

so that a quiescent truncation radius $R_{T,\rm q} = 4.73R_\star$ (corotation radius) would shrink to $R_{T,\rm out} = 1.45R_\star$ during the outburst. Such strong inward motion has two immediate observational consequences. First, material accreting very close to the stellar surface produces a dense permitted-line spectrum and strong veiling; the observed emergence of a rich emission-line forest at outburst peak that fades in quiescence (Figure 3) is therefore consistent with substantial magnetospheric compression during outburst. Second, if the bulk of accretion proceeds from these small radii, the decay time is set by the (shorter) viscous time at $R_{T,\rm out}$, and the burst would be correspondingly shorter than a TI event that drains a larger-radius annulus.

4.3.6. Mid-IR Color Evolution and Hybrid Interpretation

The observed mid-IR color evolution—becoming redder during the outburst (Section 3.6)—indicates that the disk itself is heated and contributes strongly to the mid-IR flux (see Section 4.4). This behavior favors a disk-origin heating (i.e., TI) as the primary driver of the luminosity increase, rather than a strictly magnetospheric (stellar-surface) burst.

Taken together with the spectral evidence for magnetospheric compression, the data favor a hybrid interpretation in which a thermally driven enhancement of disk accretion (TI) provides the primary energy and mass release, while magnetospheric effects (DS-like gated accretion or partial truncation collapse) operate during the peak and shape the spectral signatures. We therefore present TI as the more plausible primary mechanism for the 2024 event, with DS effects providing a complementary role; the shorter 2019 event may require different hot-state parameters or a more dominant DS contribution.

4.3.7. Clump-mediated Episodic Accretion: A Natural Route to Variable Inner-disk Mass

The inferences in Section 4.3.4 argue against steady, uniform accretion supplying $M_{\rm critical}$ and instead favor an episodic accumulation of material in the inner disk. A very natural physical channel for such behavior is the formation and inward migration of dense clumps (or vortices) that act as transient mass reservoirs. Large-scale (magneto)hydrodynamical instabilities, e.g., Rossby-wave instabilities, zonal flows, or vertical-shear instabilities, readily generate long-lived pressure traps and vortices that concentrate gas and solids and can produce planet-scale clumps at radii comparable to $r_{\rm trigger}$ (R. V. E. Lovelace et al. 1999; A. Johansen et al. 2009;

N. Manger et al. 2020, and references therein). Such structures offer a robust way to collect similar amounts of mass repeatedly: Vortices have a quasi-equilibrium geometry that tends to set the trapped mass and density contrast, and migration or tidal stripping of these clumps can then deliver a comparable mass to the inner disk in each episode.

Finally, clump infall also provides a natural explanation for the shape of the 2024 event: The first phase (until day 118 in Figure 4) can be powered by the same mechanism that piled-up matter in the 2019 outburst, while the prolonged tail (after day 205 in Figure 4) could be sustained by episodic delivery of additional clumps or fragments. We therefore consider clump-mediated, episodic mass delivery to be a very plausible—and physically motivated—mechanism for producing the observed repeating outbursts.

4.4. Mid-infrared Reddening during the Outburst: Consequence of Viscous/Irradiated Disk

It has long been observed that YSOs become optically bluer as their brightness increases (Á. Kóspál et al. 2011; D. Lorenzetti et al. 2012); however, MIR colors have shown myriad features during brightening events (W. Park et al. 2021). This behavior has been attributed to a combination of an increase in circumstellar extinction and changes in the intrinsic color of the disk (H. Liu et al. 2022).

Enhanced extinction suppresses shorter-wavelength fluxes more than those at longer wavelengths. This might explain the reddening of YSOs at MIR wavelengths during outbursts; however, the contemporaneous blueing in the optical wavelengths is in sharp contrast to the extinction.

H. Liu et al. (2022) modeled the optical and MIR color evolution of a star-disk system during an increase in the accretion rate. The authors modeled the star and disk using BT-Settl spectra at corresponding temperatures, and with a hotspot modeled as a blackbody of 8000 K. The disk temperature was estimated from a combination of irradiation and viscous heating. The MIR evolution from this model showed that the color initially reddens with increasing mass-accretion rate, and later turns blue. Since the time resolution of NEOWISE is insufficient to trace the full locus (from Figure 16 in H. Liu et al. 2022), the effective color change observed during an outburst would depend on both the initial accretion rate and the accretion rate change during the outburst.

We modeled the emission from the Gaia24ccy system across the outburst. Instead of implementing a sophisticated model like that of H. Liu et al. (2022), we modeled the system with a set of blackbodies and calculated the optical and MIR light curves from quiescence to outburst (see Figure 8). The model is described in detail in Appendix D.

The results of the model are shown in Figure 8. The first row shows the optical ($g-r$) and MIR (W1 − W2) color–magnitude evolution as the mass-accretion rate increases from $10^{-9}\,M_\odot\,\mathrm{yr}^{-1}$ during quiescence to $1.9\times10^{-7}\,M_\odot\,\mathrm{yr}^{-1}$ during the outburst peak. Colored dots represent Gaia24ccy B, while the gray curve highlights the evolution of the combined flux, Gaia24ccy A +Gaia24ccy B. Initially, Gaia24ccy B and the combined Gaia24ccy system become optically bluer as the mass-accretion rate increases. However, both exhibit a sharp turn and begin to redden at accretion rates of $\dot{M}_{\rm acc}=5.7$ and $7\times10^{-8}\,M_\odot\,\mathrm{yr}^{-1}$, respectively. The MIR color evolution shows an intriguing profile: The system initially reddens as the mass-accretion rate increases, then undergoes a sharp transition to bluer colors above

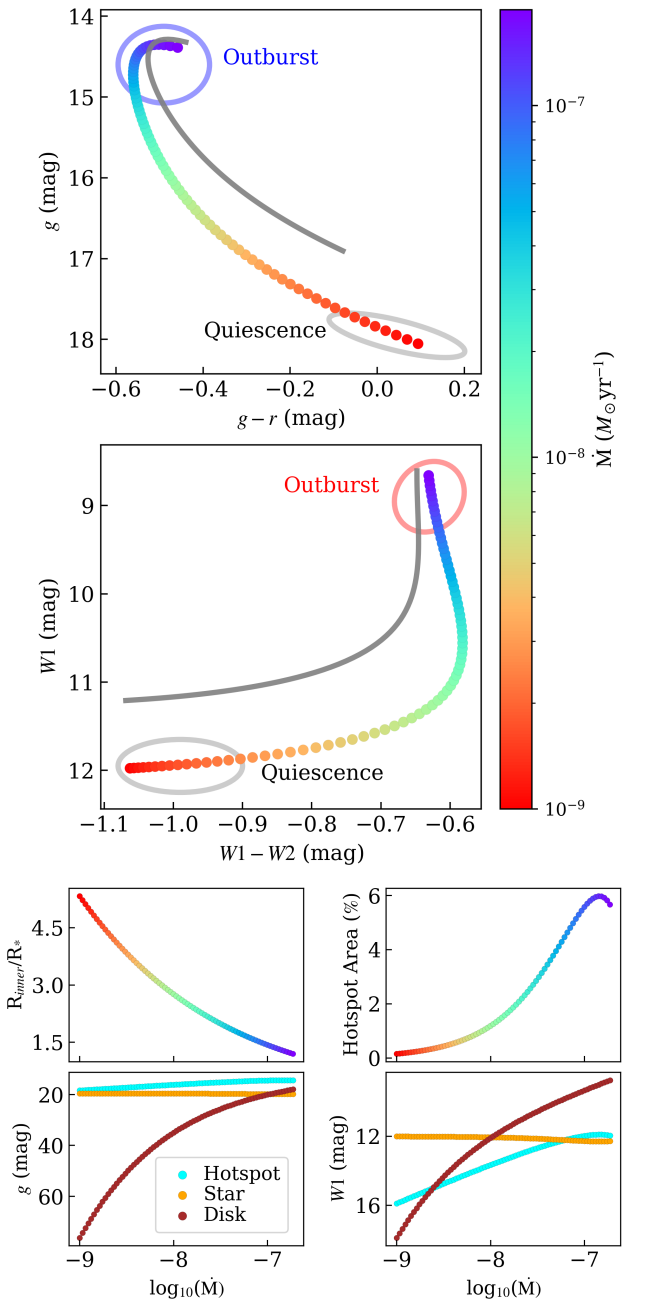

Figure 8. Results from a viscous disk model with mass-accretion rate varying from 1×10^{-9} to $1.9\times10^{-7}\,M_\odot\,\mathrm{yr}^{-1}$. The top two plots show the optical (upper) and MIR (middle) color–magnitude evolution for Gaia24ccy B (colored dots) and the Gaia24ccy system (gray curve). Fluxes were converted to magnitudes with arbitrary zero-points to mimic observations. The color bar maps the accretion rate to the color of the dots. The third row shows the evolution of the inner disk radius (left) in terms of stellar radius and fractional area of the stellar surface covered by the hotspot (right). The bottom row highlights the contribution of the star, hotspot, and disk to the optical (left) and MIR (right) fluxes of Gaia24ccy B.

accretion rates of $\dot{M}_{\rm acc}=2$ and $4.6\times10^{-8}\,M_\odot\,\mathrm{yr}^{-1}$ for Gaia24ccy B and Gaia24ccy, respectively. This suggests that if the objects had been accreting at a rate higher by an order of magnitude during quiescence, the outburst would likely have shown objects becoming bluer in the MIR. The optical reddening might not be observed at these high accretion rates, given the intrinsic variability in the observed colors. This may provide a qualitative explanation for the results of C. Morris et al. (2025),

who found that a larger fraction of class II objects show MIR reddening during an outburst, whereas most class I objects demonstrate MIR blueing.

Figure 8 shows that the optical color changed by $\Delta(g-r) = -0.55$ mag for Gaia24ccy B and by $\Delta(g-r) = -0.36$ mag for Gaia24ccy, both of which differ from the observed $\Delta(g-r) = -0.85$ mag (Section 3.6). This discrepancy may reflect the large spread in the observed color change (Figure 7). The modeled MIR color change during the outburst is $\Delta(W1-W2) = 0.43$ mag for Gaia24ccy B and 0.42 mag for Gaia24ccy, in good agreement with the observed value of $\Delta(\mathrm{W1}-\mathrm{W2}) = 0.33$ mag. This suggests that the MIR-emitting regions, primarily the two disks, have similar physical conditions. However, the optical flux-emitting regions, hotspots, and photospheres may differ between the two objects. Therefore, we must caution against overinterpreting this simplistic toy model of the Gaia24ccy system.

The middle row of Figure 8 shows the evolution of the inner disk radius in units of stellar radius and the fractional area of the stellar surface covered by the hotspot. The bottom row shows the flux contribution in the optical (g) and MIR (W1) bands from each of the individual components of Gaia24ccy B: the star, hotspot, and disk. The hotspot dominates at optical wavelengths; however, in the MIR, the disk outshines the central star at accretion rates higher than $\dot{M}_{\rm acc} = 10^{-8}\,M_\odot\ \mathrm{yr}^{-1}$, similar to the accretion rate at which Gaia24ccy B transitions to bluer MIR colors. This indicates that the MIR reddening is a consequence of competition between the emission from the disk and stellar photosphere. The disk also outshines the hotspot in the MIR at accretion rates higher than $2.5 \times 10^{-9}\,M_\odot\ \mathrm{yr}^{-1}$.

5. Conclusion

We performed a detailed photometric study of the intriguing system Gaia24ccy, with two closely matched outbursts $\Delta g = 3.8$ mag outbursts at an interval of $\sim$5 yr, in 2019 and 2024. The system also showed a rising MIR trend and $\Delta V = 1$ mag bump in 2014, likely indicating a missed outburst or a regular variability. The system comprises two fast-rotating objects, Gaia24ccy A and Gaia24ccy B, with rotation periods of $P_{\rm A} = 1.1419$ and $P_{\rm B} = 1.7898$ days, respectively. The pronounced appearance of Gaia24ccy B's periodic signal just before the 2019 and 2024 outbursts, together with increases in both the mean and peak-to-peak flux levels, indicates that the outbursting object was Gaia24ccy B. This established Gaia24ccy B as a YSO. Gaia24ccy A appears to be a quasiperiodic dipper, suggesting it is a highly inclined YSO. Gaia24ccy B underwent accretion-rate enhancements by factors of $\sim$67 and $\sim$61 during the 2019 and 2024 outbursts, respectively. The two outburst profiles display a remarkable repeatability: both rose at the same rate over the first 15 days, dipped, and remained at $g \sim 13$ mag until day 80. This was followed by a sharp dip at day 100. Both outbursts exhibited multiple subbursts on timescales of 5–25 days, likely regulated by disk processes. The 2019 outburst lasted 145–255 days, whereas the 2024 outburst persisted for 367 days.

The similarity of the outburst profiles during the rise and most of the decay, together with the similar amounts of mass accretion, constrains the trigger mechanism to either TI or DS. By comparing the thermal and viscous timescales to the rise and decay timescales of the two outbursts, we estimated the disk scale height ratio (h). For the 2024 outburst, $h = 0.10$–0.16, which appears plausible for a hot, puffed-up disk. However, reconciling this with the 2019 event would require either a more strongly puffed-up disk ($h = 0.16$–26) or a smaller trigger radius, $r_{\rm trigger}$. Assuming a plausible hot-disk value of $\alpha \in (0.10$–$0.15)$, we find the unstable region of the disk to be compact, $5.0R_\star$ ($\equiv 0.019$ au) $\leqslant r_{\rm trigger} \leqslant 12.3R_\star$ ($\equiv 0.047$ au). The mean surface density of the disk estimated from the total accreted mass does not clearly distinguish between TI and DS. The timescales of the events, the emergence of emission lines, and the MIR reddening during outburst suggest that the 2024 event was disk driven, plausibly TI, aided by DS during the peak of the outburst. However, DS appears the more dominant mechanism for the 2019 outburst.

Table 3
Summary of the Gaia24ccy B Outbursts

Parameter	Values
Time of outburst	2019 May and 2024 June
Outburst duration	145–255 days and 367 days
Outburst magnitude	$\Delta g = 3.8$ mag
Outburst peak acc. rate	$1.7 \times 10^{-7}\,M_\odot\ \mathrm{yr}^{-1}$
Quiescence acc. rate	$2.3 \times 10^{-9}\,M_\odot\ \mathrm{yr}^{-1}$
Mass accumulated (2019)	$6.5 \times 10^{-6}\,M_\odot$
Mass accumulated (2024)[a]	$7.5 \times 10^{-6}\,M_\odot$
Mass accumulated (2024)[b]	$1.3 \times 10^{-5}\,M_\odot$
Disk radius involved	$r_{\rm trigger} \sim 0.019 - 0.047$ au
Critical mass for outburst	$7.6 \times 10^{-6}\,M_\odot$
Acc. rate at $r > r_{\rm trigger}$[c]	$1.5 \times 10^{-6}\,M_\odot\ \mathrm{yr}^{-1}$
Possible cause of outburst	Pileup at $r_{\rm trigger}$ by inhomogeneous accretion at $r > r_{\rm trigger}$

Notes.
[a] Mass accumulated in the duration; same as that of 2019.
[b] Mass accumulated in the entire 2024 outburst duration.
[c] Assuming uniform accretion rate at $r > r_{\rm trigger}$.

The mass reservoir provided an estimation of steady mass inflow rate beyond the trigger radius, $\dot{M}_{r>r_{\rm trigger}} = 2 \times 10^{-6}\,M_\odot\ \mathrm{yr}^{-1}$. $\dot{M}_{r>r_{\rm trigger}}$ exceeds the peak mass-accretion rate onto the star during the outbursts, suggesting that the mass inflow beyond $r_{\rm trigger}$ is inhomogeneous.

The Gaia24ccy system exhibited MIR reddening during the rise of the 2019 outburst, while simultaneously turning bluer in the optical. We modeled the system using set of blackbodies representing the star, hotspot, and disk. The spectral energy distribution reproduces the observations when the model accretion rate is increased from the observed quiescent-state value to that of the outburst state. The model demonstrates that the observed MIR reddening is driven by emission from the inner disk dominating over the contribution from the central star. This further provides a qualitative explanation for the findings that the MIR colors of most class I objects become bluer during outbursts, whereas class II objects mainly turn redder.

We recommend continued monitoring of Gaia24ccy. Confirmation of another outburst in 2029 will be critical for establishing the 5 yr periodicity of the outbursts. Future spatially resolved spectroscopy would enable improved characterization of both stellar objects. Spatially resolved photometry will be essential for understanding the binarity of the system, for its position angle might have evolved. High-resolution ALMA observations will be crucial to determine whether the disks are circumstellar or circumbinary, and whether they are misaligned.

We conclude by tabulating our findings in Table 3 and by presenting a schematic of the Gaia24ccy system in Figure 9,

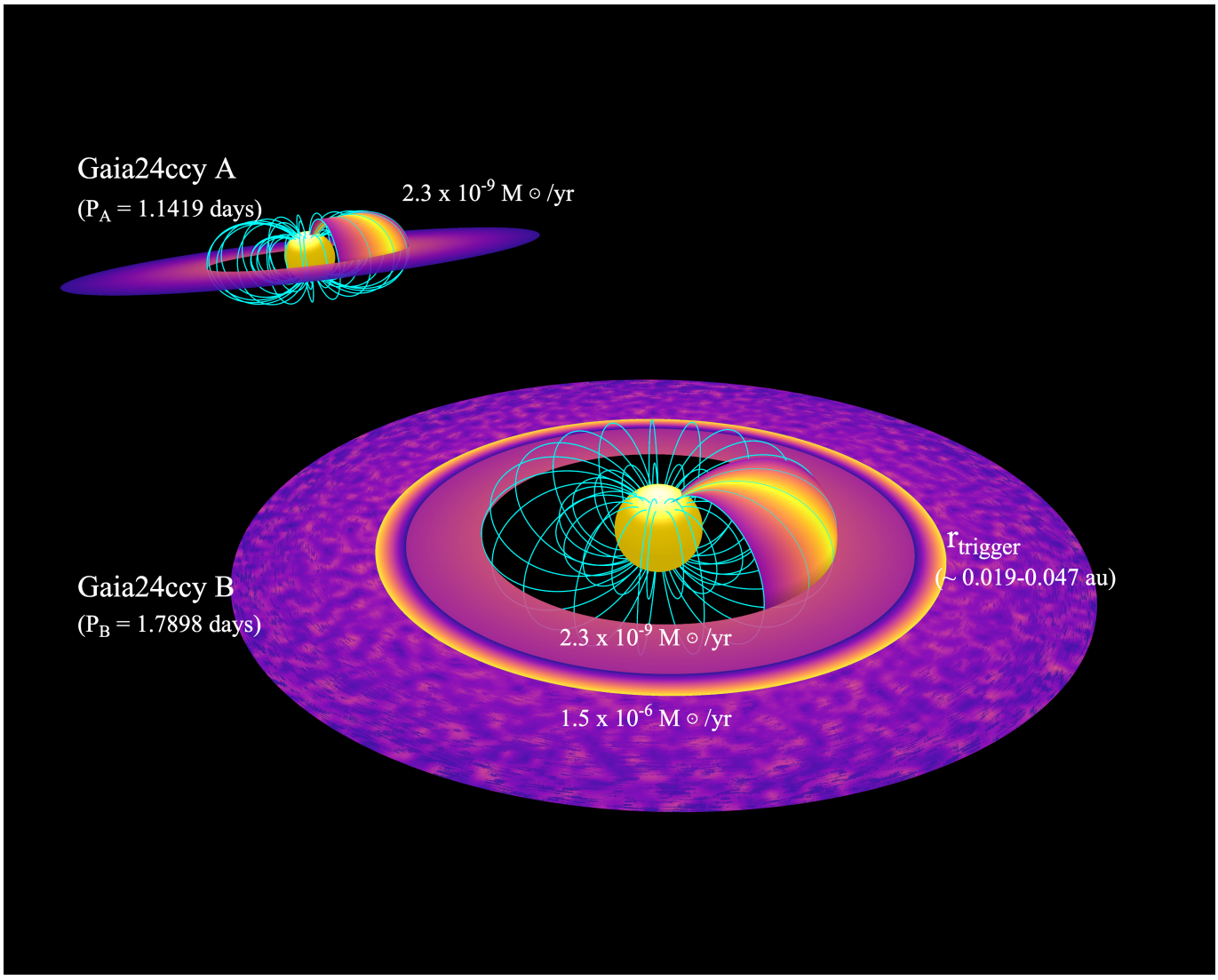

Figure 9. Schematic picture of the Gaia24ccy system depicting two closely spaced YSOs (Section 4.1): Gaia24ccy A and Gaia24ccy B (Appendix A). Gaia24ccy A has a rotation period of $P_A = 1.1419$ days and is inclined nearly edge-on, 86° (Appendix C). It is accreting at a rate of $2.3 \times 10^{-9}\,M_\odot\,\mathrm{yr}^{-1}$ (Sections 3.1 and 3.2). Gaia24ccy B, shown in the foreground, has a rotation period of $P_B = 1.7898$ days. Its inclination angle is unknown; we therefore adopt an average value of 57°. The accretion rates at the outer and inner disk may differ (Sections 3.2 and 4.3.4). Gaia24ccy B accretes at a quiescent rate of $2.3 \times 10^{-9}\,M_\odot\,\mathrm{yr}^{-1}$ from the inner disk. However, farther out in the disk, a higher, approximately uniform accretion rate of $2 \times 10^{-6}\,M_\odot\,\mathrm{yr}^{-1}$ would lead to a pileup of matter at a trigger radius $r_{\mathrm{trigger}} \sim 0.019$–$0.047$ au (Sections 4.2.1 and 4.3.3). However, accretion at $r > r_{\mathrm{trigger}}$ may be inhomogeneous, helping to limit the finite duration of the outbursts (Section 4.3.7). This inhomogeneity could take the form of clumps, as illustrated in the figure. The piled-up matter would reach a critical mass ($M_{\mathrm{critical}} = 7.6 \times 10^{-6}\,M_\odot$) in ~5 yr, thus triggering an accretion outburst (Section 4.2.1).

depicting two disk-bearing YSOs, one at the foreground undergoing outburst and the other in the background remaining quiescent.

Acknowledgments

We are thankful to the reviewer for the detailed and constructive feedback that helped us improve the clarity and quality of the paper. We thank Prof. Jerome Bouvier for the discussion on the dippers. K.S., J.P.N., and D.K.O. acknowledge the support of the Department of Atomic Energy, Government of India, under Project Identification No. RTI 4002. K.S. acknowledges the financial assistance from the Science & Engineering Research Board (SERB), Government of India, for this work, supported by grant No. ITS/2024/004263. K.S. acknowledges the Infosys-TIFR Leading Edge Travel grant. This research was supported in part by a generous donation (from the Murty Trust) aimed at enabling advances in astrophysics through the use of machine learning. The Murty Trust, an initiative of the Murty Foundation, is a not-for-profit organization dedicated to the preservation and celebration of culture, science, and knowledge of systems born out of India. The Murty Trust is headed by Mrs. Sudha Murty and Mr. Rohan Murty. This work is supported by the China–Chile Joint Research Fund (CCJRF No.2301) and the Chinese Academy of Sciences South America Center for Astronomy (CASSACA) Key Research Project E52H540301. Z.G., R.K., J.B., and J.O. are funded by ANID, Millennium Science Initiative, AIM23-001. Z.G. and C.M. are funded by the project ALMA-ANID 31240014. J.B. and R.K. thank the support from FONDECYT Regular project No. 1240249. This work is supported by the Fundamental Fund of Thailand Science Research and Innovation (TSRI) through the National Astronomical Research Institute of Thailand (Public

Organization; grant No. FFB680072/0269). V.E. acknowledges support from the Ministry of Science and Higher Education of the Russian Federation (State assignment in the field of scientific activity 2023, grant No. GZ0110/23-10-IF). We thank the staff at IAO, Hanle, and CREST, Hosakote, operated by the Indian Institute of Astrophysics, Bengaluru (India), for their support in facilitating these observations. This paper includes data gathered from the Three-hundred Milli-Meter Telescope (TMMT) and the Las Campanas Remote Observatory (LCRO) located at Las Campanas Observatory, Chile. We thank Barry Madore for initiating the TMMT project. This research is based on observations made with the Thai Robotic Telescope under program ID TRTC12A_013, which is operated by the National Astronomical Research Institute of Thailand (Public Organization). This work makes use of observations from the Las Cumbres Observatory Global Telescope network.

Appendix A
Two Photometric Periods in the K2 Light Curve

L. M. Rebull et al. (2018) reported a stellar rotation period of 1.1427 days for Gaia24ccy based on analysis of the K2 light curve obtained between 2014 August 24 and 2014 November 11. This observing window is immediately after the "2014 burst/outburst?" bump shown in Figure 1.

We independently performed a Lomb–Scargle periodogram analysis of the same K2 light curve. The resulting power spectrum showed two prominent peaks within 1–3 days, at $P_A = 1.1419$ and $P_B = 1.7898$ days, with no significant peaks detected out to 15 days. The false-alarm probabilities (FAPs) of both periods are effectively zero. Both periods fold the light curve well (Figure 10). The phase-folded light curve at P_A is nearly sinusoidal, whereas at P_B it appears sinusoidal for roughly half of the rotation cycle before flattening (Figure 10).

Indeed, the K'-band AO image of the system revealed two photometrically similar ($\Delta K = 0.26$ mag) pointlike objects in close proximity (S. A. Barenfeld et al. 2019). The projected angular separation between the objects is 138.4 ± 1.8 mas, corresponding to 19.7 au. We therefore associate the two measured periods with these two components. Hereafter, we refer to the first object as Gaia24ccy A, with P_A the rotation period, and the second object as Gaia24ccy B, with P_B the rotation period. The combined system, Gaia24ccy A +Gaia24ccy B, will be referred to as Gaia24ccy. Figure 2 shows the AO image from S. A. Barenfeld et al. (2019). In the absence of spatially resolved time-series photometry, we cannot determine whether the upper object in Figure 2 corresponds to Gaia24ccy A or B, or whether it is the lower object.

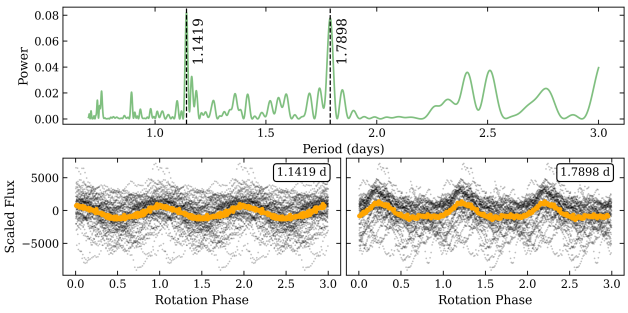

Figure 10. Upper panel: Lomb–Scargle power spectrum of the K2 light curve. The two peaks at $P_A = 1.1419$ days and $P_B = 1.7898$ days are marked with black dashed vertical lines. Lower panel: K2 light curve phase-folded at both periods (gray dots). Orange points show the running median of the folded points.

Appendix B
Appearance of P_B Just before the Outbursts: Identifying Gaia24ccy B as the Outbursting Component

ASAS-SN observed Gaia24ccy across several observation windows,[32] from 2014 May 7 to the quiescent phase following the 2024 outburst. We analyzed the Lomb–Scargle periodogram for each window separately (see Figure 11). The power spectra, 1% FAP levels, and phase-folded light curves for each window are shown in Figure 11. Although ASAS-SN light curves are sparse for such short-period objects, they recovered the rotation periods found in the K2 light curve. Periods within 0.05 days of 1 day were excluded to mitigate aliasing from the daily sampling cadence. Periodic signals from the phase-folded light curves are evident in a few windows, marked a ($P = 2.268$ days), b ($P = 1.7796$ days), f (1.7784 days), k (1.7796 days), and probably h ($P = 2.282$ days). A power spectrum peak around P_B appears in almost every window, but only in windows b, f, and k does it exceed the 1% FAP threshold. Likewise, the light curves folded at P_B are also only periodic in these certain windows, Windows f and k, with periods similar to that of Gaia24ccy B, were observed just before the 2019 and 2024 outbursts (see Figures 1 and 11). Window b, with a period similar to P_B, was observed immediately after the "2014 outburst?", while no such periodic signal appears in window g, observed immediately after the 2019 outburst. The maximum difference between the periods in windows b, f, and k and P_B is only 2° of stellar rotation, indicating that these signals likely correspond to Gaia24ccy B. Thus, the preferential appearance of a $\approx P_B$ period just before the 2019 and 2024 outbursts suggests that Gaia24ccy B is the outbursting object. Spatially resolved observations would be required to confirm this identification unambiguously.

The appearance of P_B in windows f and k may indicate an initial accretion-driven brightening of the star even before the apparent onset of the outbursts. We indeed found that both the peak-to-peak intrinsic variability and the mean flux level increased in windows f and k compared to previous windows. Specifically, the median flux levels (and peak-to-peak flux) in windows f and k were 2.45 (1.96) mJy and 2.24 (1.79) mJy, respectively, while those in the preceding windows, e and j, were 2.13 (1.23) mJy and 1.69 (1.25) mJy, respectively. A slight increase in the accretion rate before the actual onset of the outburst would enhance the hotspot contribution to the photometric flux, increasing both the peak-to-peak photometric value and the mean photometric level. These observations suggest that the accretion rate began to increase even before the actual onset of the outbursts. This could potentially help trace, anticipate, and prepare for upcoming outbursts. From here onwards, we consider Gaia24ccy B as the outbursting object, while Gaia24ccy A remains quiescent.

The power spectra also show periods ~2.28 days in almost every window. However, the power spectra peaks corresponding to period ~2.28 days exceed 1% FAP only in windows

[32] The term "window" indicates a full observation span before the star moves behind the Sun.

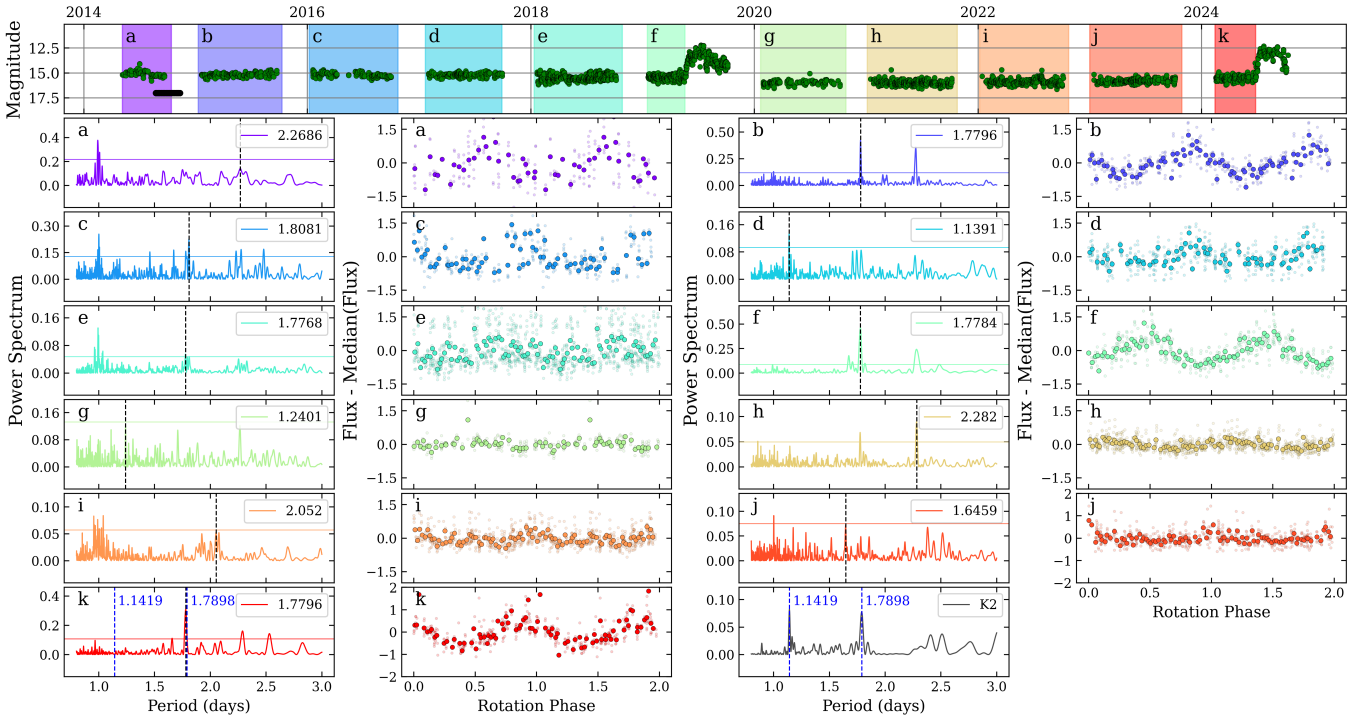

Figure 11. Lomb–Scargle periodogram analysis of ASAS-SN *g*- and *V*-band light curves of Gaia24ccy. Top row: the combined ASAS-SN *V*- and *g*-band light curves are shown by green dots. Shaded time windows indicate portions analyzed for periodicities separately. Bottom panels: sets of adjacent panels show the Lomb–Scargle power spectrum and corresponding phase-folded light curve over two rotations. Letters in the shaded regions of the light curve and power spectrum mark the corresponding windows. A 1% FAP level is indicated by a horizontal line in each power spectrum. Vertical dashed black lines mark the recovered periods, which are also indicated at the top-right corner of each respective power spectrum. The power spectra of the K2 light curve from Figure 10 are shown in the lower-right panel, with P_A and P_B marked for reference. The same two periods are also highlighted with vertical dashed blue lines in the lower-left panel. The phase-folded light curves are shown with faint dots, and their running medians are shown as brighter dots.

where power spectra peaks at $\approx P_B$ are above 1% FAP. Indeed, sampling a sine function with period P_B onto the ASAS-SN epochs of Figure 11 produces two peaks, P_B and ∼2.28 days, indicating that the latter is an alias of P_B.

Interestingly, periods corresponding to P_A are nearly absent in all windows, except for window d ($P = 1.139$ days), and even there the phase-folded light curve does not show a clear periodic signal. To understand the possible reasons for this absence of P_A in Figure 11, we generated synthetic light curves by adding two sine curves with periods P_A and P_B, while varying amplitude, SNR, and relative phase. We found that the power spectrum peak at P_A disappears when the peak-to-peak amplitude of Gaia24ccy A is $\leqslant$40% that of Gaia24ccy B. This could be indicative of differences in either accretion rate or inclination angle of the two stars, both affecting the hotspot luminosity and thus the optical peak-to-peak amplitude. We assumed similar quiescent accretion rates for both objects but adopted different inclination angles (see Sections 3.2 and 4.4). We used an average inclination angle of 57° for Gaia24ccy B, and a high inclination angle of 86° for Gaia24ccy A, following S. A. Barenfeld et al. (2017) and Appendix C.

Appendix C
Dips in the K2 Light Curve: Possibility of Gaia24ccy A as a Disk-bearing YSO

The K2 light curve of Gaia24ccy displays occasional dips, as shown in Figure 12. We searched for periodicity in these events. In the top panel of Figure 12, red dotted vertical lines are plotted at intervals of P_A, the rotation period of Gaia24ccy A (see Appendix A). The first line is phase-shifted to maximize the number of lines overlapping with the dips, and the overlapping lines are highlighted in blue. The major dips align with this period; however, their minima do not consistently align, and further not every rotation cycle exhibits a dip. To help identify periodicity in the dips, we detrended the light curve using its 85th percentile smoothed continuum, shown as a gray curve in the upper panel of Figure 12. The flux values in the detrended light curve were set to zero except during dips (see second row in Figure 12). Green dotted vertical lines, spaced at intervals of P_B, the rotation period of Gaia24ccy B, are overplotted; however, these do not coincide with several prominent dips. The third row of Figure 12 shows the fractional percentage of flux decrement during the dips (red curve). The light curve exhibits a flux decrease of up to 30% relative to the baseline. Assuming equal photometric contributions from both objects, this corresponds to a dip of up to 60% for a single object. The dips often extend beyond a full rotation cycle of Gaia24ccy A.

The dips in the continuum-detrended light curve (second row) were phase-folded at both periods and are shown in the bottom panel of Figure 12. When folding at P_A, the light curve shows stable dips, whereas the dip features are smeared out when folding at P_B. A running median of the folded light curves, shown as red dots, further enhances the alignment of dips at P_A. Both the upper and lower panels thus indicate that the dips are associated with P_A, and so with Gaia24ccy A. The Lomb–Scargle periodogram of the dipper light curve (second row in Figure 12) over the range 0.5–5 days shows a

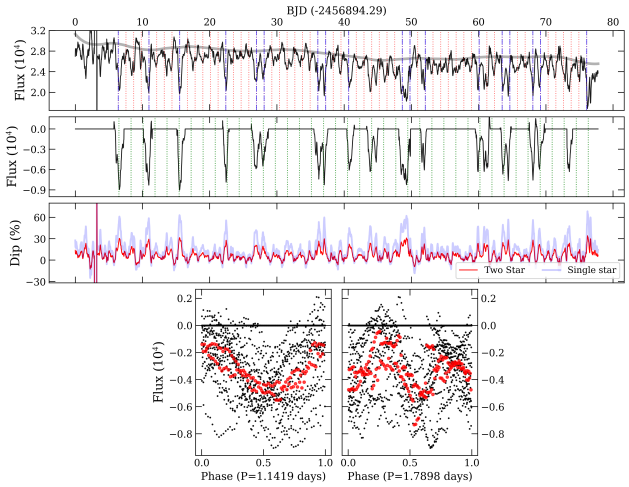

Figure 12. Dips in the K2 light curve. The upper row shows the K2 light curve with red dotted vertical lines spaced at an interval of P_A. Lines overlapping with dips are highlighted with dashed–dotted blue lines. The 85th percentile smoothed continuum of the light curve is shown as a gray curve. The second row shows the continuum-detrended light curve with flux set to zero except during dips. Dashed–dotted green vertical lines are spaced at an interval of P_B to highlight that this period misses many dips. The third row shows the fractional percentage of the total flux covered by dips (red curve). Assuming that both stars contribute equally to the total flux, the corresponding flux decrease for a single star is doubled (blue curve). The bottom row shows the phase-folded light curve from the second row, folded at P_A (left) and P_B (right), with the running median shown by red dots.

prominent peak at 4.15 days; however, the phase-folded light curve for this period is smeared. In the 0.5–2 days range, the most prominent peak occurs at $1.138 \sim P_A$, and the phase-folded light curve shows a stable dip, similar to the lower-left panel of Figure 12. The quasiperiodic nature of the dips may result from occultation by nonstable levitation of disk material at the corotation radius.

To understand the alignment of a few dips with P_B (in the second row of Figure 12), we constructed dipper light curves with 25 dips placed at random integer multiples of P_A with a 20% uncertainity. The full width at half-maximum was kept at $120^\circ \pm 30^\circ$ of the rotation of Gaia24ccy A. Across 50,000 such light curves, we found that ≈35% of dips coincided with P_B. We can see that around seven dips align with P_B out of 20 dips in Figure 12, consistent with this expectation. This suggests that, assuming the dips are associated with Gaia24ccy A, the observed alignment of a few dips with P_B is likely coincidental.

Thus, for this study, we consider the scenario of Gaia24ccy A having a highly inclined disk, where disk extinction produces quasiperiodic photometric dips.

Appendix D
Viscous Disk Model of the Gaia24ccy System

We modeled each component of the Gaia24ccy system with a set of blackbodies: a central star with a photospheric-temperature blackbody, a hotspot with a 9000 K blackbody, and a circumstellar disk represented by blackbodies from viscously heated annuli. We defined the inner disk radius (R_{in}) as the point at which the disk ram pressure balances the magnetic pressure. For $B_\star = 1$ kG, the inner disk would reach the stellar surface at an accretion rate below that of the outburst peak. We therefore used another reasonable estimate of $B_\star$ by equating the corotation radius with the truncation radius during quiescence, yielding $B_\star \approx 1.5$ kG. We also set $R_{in} = \max(R_\star, R_{in})$. The hotspot area was varied to match the luminosity with that expected from the gravitational energy released by the freefall of the accreting material from R_{in} to $R_\star$. An average inclination angle of 57° was adopted for Gaia24ccy B, and 86° for Gaia24ccy A (S. A. Barenfeld et al. 2017). We varied the mass-accretion rate and calculated the fluxes in optical and MIR bands. The fluxes were then converted to magnitudes using arbitrary zero-points to mimic the observed magnitude ranges in Figure 7. Finally, we combined the luminosities of Gaia24ccy A and Gaia24ccy B, assuming Gaia24ccy A remained in quiescence while Gaia24ccy B underwent an outburst. The results are shown in Section 4.4 and Figure 8.

ORCID iDs

Koshvendra Singh https://orcid.org/0000-0002-7434-9681
Joe P. Ninan https://orcid.org/0000-0001-8720-5612
Zhen Guo https://orcid.org/0000-0003-0292-4832
Valentin D. Ivanov https://orcid.org/0000-0002-5963-1283
David A. H. Buckley https://orcid.org/0000-0002-7004-9956
Devendra K. Ojha https://orcid.org/0000-0001-9312-3816
Andrew Monson https://orcid.org/0000-0002-0048-2586
Tarak Chand https://orcid.org/0009-0008-8490-8601
Saurabh Sharma https://orcid.org/0000-0001-5731-3057
Ram Kesh Yadav https://orcid.org/0000-0002-6740-7425
Devendra K. Sahu https://orcid.org/0000-0002-6688-0800
Vardan Elbakyan https://orcid.org/0000-0002-9433-900X
Sergei Nayakshin https://orcid.org/0000-0002-6166-2206
Vitor Fermiano https://orcid.org/0009-0003-4432-9537
Min Fang https://orcid.org/0000-0001-8060-1321
Jura Borissova https://orcid.org/0000-0002-5936-7718
Wen Ping Chen https://orcid.org/0000-0003-0262-272X
Franz-Josef Hambsch https://orcid.org/0000-0003-0125-8700
Radostin Kurtev https://orcid.org/0000-0002-9740-9974
Calum Morris https://orcid.org/0000-0002-7535-7077
Javier Osses https://orcid.org/0009-0007-6769-7075
Vania Rodríguez https://orcid.org/0009-0007-6273-9141
Tanvi Sharma https://orcid.org/0000-0003-1634-3158
Bandari Srikanth https://orcid.org/0009-0004-1054-2812
Thanawuth Thanathibodee https://orcid.org/0000-0003-4507-1710
Wei-Hao Wang https://orcid.org/0000-0003-2588-1265
Yuting Zhou https://orcid.org/0009-0004-8171-3551

References

Ábrahám, P., Juhász, A., Dullemond, C. P., et al. 2009, Natur, 459, 224
Alcalá, J. M., Manara, C. F., Natta, A., et al. 2017, A&A, 600, A20
Armitage, P. J. 2016, ApJL, 833, L15
Bailer-Jones, C. A. L., Rybizki, J., Fouesneau, M., Demleitner, M., & Andrae, R. 2021, AJ, 161, 147
Barenfeld, S. A., Carpenter, J. M., Ricci, L., & Isella, A. 2016, ApJ, 827, 142
Barenfeld, S. A., Carpenter, J. M., Sargent, A. I., Isella, A., & Ricci, L. 2017, ApJ, 851, 85
Barenfeld, S. A., Carpenter, J. M., Sargent, A. I., et al. 2019, ApJ, 878, 45
Bell, K. R., & Lin, D. N. C. 1994, ApJ, 427, 987
Bellm, E. C., Kulkarni, S. R., Graham, M. J., et al. 2019, PASP, 131, 018002
Bessell, M. S., Castelli, F., & Plez, B. 1998, A&A, 333, 231
Biddle, L. I., Johns-Krull, C. M., Llama, J., Prato, L., & Skiff, B. A. 2018, ApJL, 853, L34
Bonnell, I., & Bastien, P. 1992, ApJL, 401, L31

Borchert, E. M. A., Price, D. J., Pinte, C., & Cuello, N. 2022, MNRAS, 510, L37
Bouvier, J., Alencar, S. H. P., Harries, T. J., Johns-Krull, C. M., & Romanova, M. M. 2007, in Protostars and Planets V, ed. B. Reipurth, D. Jewitt, & K. Keil, 479 (Univ. of Arizona Press)
Bouvier, J., Chelli, A., Allain, S., et al. 1999, A&A, 349, 619
Brown, T. M., Baliber, N., Bianco, F. B., et al. 2013, PASP, 125, 1031
Calvet, N., & Gullbring, E. 1998, ApJ, 509, 802
Cardelli, J. A., Clayton, G. C., & Mathis, J. S. 1989, ApJ, 345, 245
Claes, R. A. B., Campbell-White, J., Manara, C. F., et al. 2024, A&A, 690, A122
Cuello, N., Ménard, F., & Price, D. J. 2023, EPJP, 138, 11
D'Angelo, C. R., & Spruit, H. C. 2012, MNRAS, 420, 416
David, T. J., Hillenbrand, L. A., Gillen, E., et al. 2019, ApJ, 872, 161
Dubus, G., Hameury, J.-M., & Lasota, J.-P. 2001, A&A, 373, 251
Fang, M., Kim, J. S., Pascucci, I., et al. 2017, AJ, 153, 188
Fang, M., Pascucci, I., Edwards, S., et al. 2018, ApJ, 868, 28
Fang, M., Pascucci, I., Edwards, S., et al. 2023, ApJ, 945, 112
Feiden, G. A. 2016, A&A, 593, A99
Fischer, W. J., Hillenbrand, L. A., Herczeg, G. J., et al. 2023, ASPC, 534, 355
Förster, F., Cabrera-Vives, G., Castillo-Navarrete, E., et al. 2021, AJ, 161, 242
Gaia Collaboration, Vallenari, A., Brown, A. G. A., et al. 2023, A&A, 674, A1
Gullbring, E., Barwig, H., Chen, P. S., Gahm, G. F., & Bao, M. X. 1996, A&A, 307, 791
Gullbring, E., Hartmann, L., Briceño, C., & Calvet, N. 1998, ApJ, 492, 323
Guo, Z., Herczeg, G. J., Jose, J., et al. 2018, ApJ, 852, 56
Guo, Z., Lucas, P. W., Smith, L. C., et al. 2022, MNRAS, 513, 1015
Hameury, J.-M., Menou, K., Dubus, G., Lasota, J.-P., & Hure, J.-M. 1998, MNRAS, 298, 1048
Herczeg, G. J., & Hillenbrand, L. A. 2008, ApJ, 681, 594
Herczeg, G. J., & Hillenbrand, L. A. 2014, ApJ, 786, 97
Ingleby, L., Calvet, N., Bergin, E., et al. 2011, ApJ, 743, 105
Ioannidis, G., & Froebrich, D. 2012, MNRAS, 425, 1380
Johansen, A., Youdin, A., & Klahr, H. 2009, ApJ, 697, 1269
Kenyon, S. J., Hartmann, L. W., Strom, K. M., & Strom, S. E. 1990, AJ, 99, 869
Kochanek, C. S., Shappee, B. J., Stanek, K. Z., et al. 2017, PASP, 129, 104502
Kóspál, Á., Ábrahám, P., Acosta-Pulido, J. A., et al. 2011, A&A, 527, A133
Kóspál, Á., Ábrahám, P., Zsidi, G., et al. 2018, ApJ, 862, 44
Kuffmeier, M., Frimann, S., Jensen, S. S., & Haugbølle, T. 2018, MNRAS, 475, 2642
Landolt, A. U. 1992, AJ, 104, 340
Liu, H., Herczeg, G. J., Johnstone, D., et al. 2022, ApJ, 936, 152
Lorenzetti, D., Antoniucci, S., Giannini, T., et al. 2012, ApJ, 749, 188
Lovelace, R. V. E., Li, H., Colgate, S. A., & Nelson, A. F. 1999, ApJ, 513, 805
Mainzer, A., Bauer, J., Grav, T., et al. 2011, ApJ, 731, 53
Manara, C. F. 2014, PhD thesis, Ludwig-Maximilians Univ. of Munich, Germany
Manara, C. F., Frasca, A., Alcalá, J. M., et al. 2017, A&A, 605, A86
Manara, C. F., Natta, A., Rosotti, G. P., et al. 2020, A&A, 639, A58
Manara, C. F., Testi, L., Rigliaco, E., et al. 2013, A&A, 551, A107
Manger, N., Klahr, H., Kley, W., & Flock, M. 2020, MNRAS, 499, 1841
Menou, K., Esin, A. A., Narayan, R., et al. 1999, ApJ, 520, 276
Monson, A. J., Beaton, R. L., Scowcroft, V., et al. 2017, AJ, 153, 96
Morris, C., Guo, Z., Lucas, P. W., et al. 2025, MNRAS, 537, 2763
Muñoz, D. J., & Lai, D. 2016, ApJ, 827, 43
Nagel, E., Bouvier, J., & Duarte, A. E. 2024, A&A, 688, A61
Nayakshin, S., Cruz Sáenz de Miera, F., Kóspál, Á., et al. 2024, MNRAS, 530, 1749
Nayakshin, S., & Elbakyan, V. 2024, MNRAS, 528, 2182
Nayakshin, S., & Lodato, G. 2012, MNRAS, 426, 70
Onken, C. A., Wolf, C., Bessell, M. S., et al. 2024, PASA, 41, e061
Pancino, E., Marrese, P. M., Marinoni, S., et al. 2022, A&A, 664, A109
Park, W., Lee, J.-E., Contreras Peña, C., et al. 2021, ApJ, 920, 132
Pecaut, M. J., Mamajek, E. E., & Bubar, E. J. 2012, ApJ, 746, 154
Rebull, L. M., Stauffer, J. R., Cody, A. M., et al. 2018, AJ, 155, 196
Sánchez-Sáez, P., Reyes, I., Valenzuela, C., et al. 2021, AJ, 161, 141
Shappee, B. J., Prieto, J. L., Grupe, D., et al. 2014, ApJ, 788, 48
Singh, K., Ninan, J. P., Romanova, M. M., et al. 2024, ApJ, 968, 88
Smith, L. C., Lucas, P. W., Koposov, S. E., et al. 2025, MNRAS, 536, 3707
Smith, L. C., Lucas, P. W., Kurtev, R., et al. 2018, MNRAS, 474, 1826
Sokolovsky, K., Korotkiy, S., Potapov, N., & Ostapenko, S. 2024, ATel, 16696, 1
Testi, L., Natta, A., Manara, C. F., et al. 2022, A&A, 663, A98
Teyssandier, J., & Lai, D. 2020, MNRAS, 495, 3920
Tody, D. 1986, SPIE, 627, 733, 10.1117/12.968154
Tofflemire, B. M., Mathieu, R. D., Herczeg, G. J., Akeson, R. L., & Ciardi, D. R. 2017, ApJL, 842, L12
Tonry, J. L., Denneau, L., Heinze, A. N., et al. 2018, PASP, 130, 064505
Venuti, L., Bouvier, J., Flaccomio, E., et al. 2014, A&A, 570, A82
Wang, M.-T., Herczeg, G. J., Liu, H.-G., et al. 2023, ApJ, 957, 113